



City Research Online

City, University of London Institutional Repository

Citation: Wang, J. & Ma, Q. (2015). Numerical techniques on improving computational efficiency of spectral boundary integral method. *International Journal for Numerical Methods in Engineering*, 102(10), pp. 1638-1669. doi: 10.1002/nme.4857

This is the accepted version of the paper.

This version of the publication may differ from the final published version.

Permanent repository link: <https://openaccess.city.ac.uk/id/eprint/7156/>

Link to published version: <https://doi.org/10.1002/nme.4857>

Copyright: City Research Online aims to make research outputs of City, University of London available to a wider audience. Copyright and Moral Rights remain with the author(s) and/or copyright holders. URLs from City Research Online may be freely distributed and linked to.

Reuse: Copies of full items can be used for personal research or study, educational, or not-for-profit purposes without prior permission or charge. Provided that the authors, title and full bibliographic details are credited, a hyperlink and/or URL is given for the original metadata page and the content is not changed in any way.

City Research Online:

<http://openaccess.city.ac.uk/>

publications@city.ac.uk

Numerical techniques on improving computational efficiency of Spectral Boundary Integral Method

Jinghua Wang and Q.W. Ma*

School of Engineering and Mathematical Sciences, City University London, United Kingdom

**Corresponding Author Email: q.ma@city.ac.uk*

SUMMARY

Numerical techniques are suggested in this paper, in order to improve the computational efficiency of the Spectral Boundary Integral Method, initiated by Clamond & Grue [D. Clamond and J. Grue. A fast method for fully nonlinear water-wave computations. *J. Fluid Mech.* 2001; **447**: 337-355] for simulating nonlinear water waves. This method involves dealing with the high order convolutions by using Fourier Transform or Inverse Fourier Transform and evaluating the integrals with **weakly** singular integrands. A de-singularity technique is proposed here to help efficiently evaluating the integrals with **weak** singularity. An anti-aliasing technique is developed in this paper to overcome the aliasing problem associated with Fourier Transform or Inverse Fourier Transform with a limited resolution. This paper also presents a technique for determining a critical value of the free surface, under which the integrals can be neglected. Numerical tests are carried out on the numerical techniques and on the improved method equipped with the techniques. The tests will demonstrate that the improved method can significantly accelerate the computation, in particular when waves are strongly nonlinear.

KEYWORDS: nonlinear water waves; boundary integral method; de-singularity technique; anti-aliasing technique; spectral method

1. INTRODUCTION

For centuries, the gravity water wave problems have been studied extensively. In order to describe and solve the problems, various approaches have been introduced. The potential wave theory, which assumes the fluid is inviscid and irrotational, has been widely adopted in the studies of this subject. The early contributions came from pioneer researchers and their linear theories, such as Airy [5], Lamb [6], Lighthill [7] and so on. The Stokes wave theory [8] was another milestone to the wave theories. The equations derived by Boussinesq [9], and Korteweg & DE Vries [10] initiated the studies on waves in shallow water. In 1960s, when Benjamin & Feir [11] published their astonishing discovery of the existence of instability in a perturbed uniform wave train, nonlinear waves began to draw extensive attentions from researchers such as Benney & Roskes [12], Chu & Mei [13], Davey & Stewartson [14], Hasimoto & Ono [15], Dysthe [16] and so on. Besides, the impressive work of the derivation of the mode coupling equation by Zakharov [17], and his nonlinear Schrödinger equation,

opened another door for studying nonlinear water waves.

Fully nonlinear analysis did not start until the emerging of advanced computing technologies. The Boundary Element Method (BEM) was first introduced by Longuet-Higgins & Cokelet [18], who started a new era to model the fully nonlinear waves numerically. It was successfully applied to simulate two-dimensional (2D) overturning waves. The algorithm of BEM was later improved by Grilli *et al.* [19], Dold [20] and many others. Meanwhile, Wu & Eatock-Taylor [22, 23] proposed the Finite Element Method (FEM) to study the interaction between water waves and structures. This method was later extended to 3D cases by Ma [24] and Ma *et al.* [25, 26]. More recently, Yan & Ma [28, 29] and Ma & Yan [27, 30] introduced a new mesh strategy and proposed the Quasi Arbitrary Lagrangian-Eulerian Finite Element Method (QALE-FEM). The results obtained by using this method for 2D and 3D overturning and other strong nonlinear waves are impressive. On the other hand, Dommermuth & Yue [31] developed a tool, known as the Higher-Order Spectral Method (HOS), which was able to model waves effectively with the help of Fast Fourier Transform (FFT). However, this method was built on the assumption that the Taylor expansion of the velocity potential at the free surface was convergent. Due to this, the method does not work well when the waves are quite steep [31]. Nicholls [32] proposed a numerical model called Spectral Continuation Method to study the traveling water waves. In this method, the Dirichlet-Neumann operator was approximated by an assumed analytic function of the free surface elevation and was expanded into Taylor series. Due to the fact that the evaluation of the higher order terms is highly recursive and impractical, they chose to only use the 5th order in practice. As a consequence, this method is incapable to capture the higher order nonlinearities. Clamond & Grue [1] proposed a novel method based on a boundary integral method and FFT. Fructus *et al.* [4] made one step further extending this method to 3D cases. The method has been summarized by Grue & Fructus [40]. In this method, the Neumann operator was introduced and expressed in terms of the free surface and the velocity potential. The kinematic and dynamic boundary conditions were reformulated into the skew-symmetric form after applying the Fourier transform. The free surface and velocity potential are updated through integrating the equations with respect to time, which requires the velocity on the free surface. The velocity on the free surface is decomposed into convolution parts (to 3rd order in [4]) and integration parts. Convolution parts are evaluated by FFT, and the integration parts have kernels decaying quickly along the distance between the source and field points but their integrands are **weakly** singular. The property of the kernels enables the local integration to be estimated within a limited range (e.g., two characteristic wave lengths, say $X - L_0$ to $X + L_0$), instead of $(-\infty, \infty)$. Even though the integration range is carefully selected, integration parts still remain as the most time consuming parts in the whole numerical scheme. Furthermore, Grue [3] brought the formulation of the boundary integrals to convolutions up to the 7th order. With this formulation, the most expensive integration parts were neglected, which led to a very fast solution for the velocity on the free surface. Obviously, one can only do so for moderate steep waves. Based on the literature, the following issues need to be

addressed to make the method more robust and efficient:

- a) **Weak** singularity in the integrals requires to be dealt with carefully. Fructus *et al.* [4] have proposed a method for this. They suggested that the **weak** singularity was eliminated by evaluating the integrals at a shifted point $\mathbf{X} + \frac{1}{2}\Delta\mathbf{X}$, rather than at the singular point. This method was found to give good results when the grids used are sufficiently fine. However, fine grids require relatively long computational time. Ideally, the similar results can be obtained by using relatively coarse grids.
- b) Though the solutions for **removing** aliasing problems involved in the convolutions up to the 4th order have been proposed by Fructus *et al.* [4], it is found that the method did not work well for the convolutions of 5th or higher order. However, the technique of removing aliasing problems for higher-order convolutions was not proposed yet.
- c) When the boundary integrals are evaluated with the convolutions up to the 7th order and the integration parts are neglected as suggested by Grue [3], one needs to know the critical value of the free surface gradient, under which the approach with neglecting integration parts can give sufficiently accurate results but cannot do so beyond this. The critical free surface gradient deserves a study which has not been carried out yet.

This paper will present the numerical techniques to address the above issues. With these technique, the method described in [1-4] becomes more computational efficient and more robust. For convenience, the method described in [1-4] is named as Spectral Boundary Integral Method in this paper.

2. MATHEMATICAL FORMULATIONS

2.1. The prognostic equation

The fully nonlinear potential theory requires the kinematic and dynamic boundary conditions at the free surface to be satisfied. In **the** dimensionless form [31], they are

$$\frac{\partial\eta}{\partial T} = \frac{\partial\phi}{\partial Z} - \nabla\phi \cdot \nabla\eta \quad (1)$$

$$\frac{\partial\phi}{\partial T} + \eta + \frac{1}{2} \left(\nabla\phi \cdot \nabla\phi + \frac{\partial\phi^2}{\partial Z} \right) + p = 0 \quad (2)$$

where $\nabla = \frac{\partial}{\partial X} \vec{i} + \frac{\partial}{\partial Y} \vec{j}$ is the horizontal gradient operator, and η is the elevation of the free surface, ϕ is the velocity potential, p is the pressure on the free surface and $p = 0$ if it is not specified. Among the variables in the equations above, η , \mathbf{X} and Z have been non-dimensionalized by multiplying K_0 , ϕ by multiplying $\sqrt{K_0^3/g}$, p by multiplying $K_0/(\rho g)$, and T by multiplying Ω_0 . K_0 is the characteristic wave number, Ω_0 the corresponding circular frequency ($\Omega_0 = \sqrt{gK_0}$),

ρ the density of the fluid and g the gravity acceleration. The wave number of the most energetic component in the spectrum at the beginning of the simulation is chosen as the characteristic wave number K_0 . After introducing the new variable in Neumann form representing the vertical velocity, $V = \frac{\partial \phi}{\partial n} \sqrt{1 + |\nabla \eta|^2}$, where n is the normal vector of the free surface, Equation (1) and (2) become

$$\frac{\partial \eta}{\partial T} - V = 0 \quad (3)$$

$$\frac{\partial \tilde{\phi}}{\partial T} + \eta + \frac{1}{2} \left(|\nabla \tilde{\phi}|^2 - \frac{(V + \nabla \eta \cdot \nabla \tilde{\phi})^2}{1 + |\nabla \eta|^2} \right) + p = 0 \quad (4)$$

where $\tilde{\phi}$ denotes the velocity potential on the free surface $\tilde{\phi}(\mathbf{X}, T) = \phi(\mathbf{X}, Z = \eta(\mathbf{X}, T), T)$. One should note that derivatives of $\tilde{\phi}$ in Equation (3) & (4) are different from these of ϕ in Equations (1) & (2). They satisfy the relation

$$\nabla \tilde{\phi} = (\nabla \phi)|_{z=\eta} + \left(\frac{\partial \phi}{\partial Z} \right) \Big|_{z=\eta} \nabla \eta \quad (5)$$

$$\frac{\partial \tilde{\phi}}{\partial T} = \left(\frac{\partial \phi}{\partial T} \right) \Big|_{z=\eta} + \left(\frac{\partial \phi}{\partial Z} \right) \Big|_{z=\eta} \frac{\partial \eta}{\partial T} \quad (6)$$

Following [4], the Fourier transform and the inverse Fourier transform are defined as (take the velocity potential on the free surface for example)

$$\hat{\phi}(\mathbf{K}, T) = F\{\tilde{\phi}\} = \int_{S_0} \tilde{\phi}(\mathbf{X}, T) e^{-i\mathbf{K} \cdot \mathbf{X}} d\mathbf{X} \quad (7)$$

$$\tilde{\phi}(\mathbf{X}, T) = F^{-1}\{\hat{\phi}\} = \frac{1}{4\pi^2} \int_{S_0} \hat{\phi}(\mathbf{K}, T) e^{i\mathbf{K} \cdot \mathbf{X}} d\mathbf{K}$$

where \mathbf{K} is the wave number and S_0 is the projection of the whole free surface on the horizontal plane. After applying Fourier transform, Equations (3) & (4) lead to the following skew-symmetric prognostic equation

$$\frac{\partial \vec{M}}{\partial T} + A\vec{M} + \vec{R} = \vec{N} \quad (8)$$

where

$$\vec{M} = \begin{pmatrix} KF\{\eta\} \\ K\Omega F\{\tilde{\phi}\} \end{pmatrix}, \quad A = \begin{bmatrix} 0 & -\Omega \\ \Omega & 0 \end{bmatrix}, \quad \vec{R} = \begin{pmatrix} 0 \\ K\Omega F\{p\} \end{pmatrix}, \quad \vec{N} = \begin{pmatrix} KF\{G_1\} \\ K\Omega F\{G_2\} \end{pmatrix} \quad (9)$$

$$F\{G_1\} = F\{V\} - KF\{\tilde{\phi}\}$$

$$F\{G_2\} = F\left\{ \frac{1}{2} \left[\frac{(V + \nabla \eta \cdot \nabla \tilde{\phi})^2}{1 + |\nabla \eta|^2} - |\nabla \tilde{\phi}|^2 \right] \right\}$$

and $\Omega = \sqrt{K}$, $K = |\mathbf{K}|$. The solution to Equation (8) is given as

$$\vec{M}(T) = e^{-A(T-T_0)} \int_{T_0}^T e^{A(T-T_0)} (\vec{N} - \vec{R}) dT + e^{-A(T-T_0)} \vec{M}(T_0) \quad (10)$$

where

$$e^{A\Delta T} = \begin{bmatrix} \cos \Omega\Delta T & -\sin \Omega\Delta T \\ \sin \Omega\Delta T & \cos \Omega\Delta T \end{bmatrix} \quad (11)$$

According to Clamond and Fructus [33], this time integrator is linearly stable and exact. The six-stage embedded 5th order Runge-Kutta method is adopted to solve the equation numerically. The solution can be written as

$$\begin{aligned} \vec{M}^{(4)} &= e^{-A(T-T_0)} \left[\vec{M}(T_0) + \sum_{i=1}^6 \alpha_i \kappa_i \right] \\ \vec{M}^{(5)} &= e^{-A(T-T_0)} \left[\vec{M}(T_0) + \sum_{i=1}^6 \beta_i \kappa_i \right] \end{aligned} \quad (12)$$

where coefficients α_i and β_i can be found in [34], and κ_i is the Runge-Kutta increment at each stage. The superscripts (4) and (5) represent the 4th order and 5th order solution of the Runge-Kutta time integrator respectively. The time step size is self-adaptive which is determined by imposing the following condition

$$Err_T = \frac{\int [|\eta^{(5)} - \eta^{(4)}| + |\tilde{\phi}^{(5)} - \tilde{\phi}^{(4)}|] d\mathbf{X}}{\int [|\eta^{(5)}| + |\tilde{\phi}^{(5)}|] d\mathbf{X}} < Tol_T \quad (13)$$

where Err_T is the relative error between the 4th and 5th order solutions and Tol_T is the tolerance. Using the equation, one can obtain the optimised time step size ΔT_{opt} as a function of Err_T , as suggested in [33].

2.2. The boundary integral solver

One can find the solutions from Equation (10) for the wave elevation (η) and velocity potential ($\tilde{\phi}$) on the free surface if the velocity V on the free surface is given. To obtain V , one needs to solve the Laplace equation governing the velocity potential in the whole fluid domain, which can be transferred to a boundary integral equation using the Green's theorem. The procedure and methodology is well known and so details will not be given here. Only the result of the boundary integral equation in [18] is written out as follows for completeness,

$$\iint_S \frac{1}{r} \frac{\partial \phi'}{\partial n'} dS' = 2\pi\tilde{\phi} + \iint_S \tilde{\phi}' \frac{\partial}{\partial n'} \frac{1}{r} dS' \quad (14)$$

where S is the area of the instantaneous free surface, the variables with the prime indicate those at source point (\mathbf{X}', Z') , the variables without the prime are those at field point (\mathbf{X}, Z) , $r = \sqrt{R^2 + (Z' - Z)^2}$ and $R = |\mathbf{R}| = |\mathbf{X}' - \mathbf{X}|$, S' denotes the segment of $S(\mathbf{X}', Z')$. Using $dS' = \sqrt{1 + |\nabla\eta|^2} d\mathbf{X}'$, the above integral can be written

as

$$\int_{S_0} \frac{V'}{r} d\mathbf{X}' = 2\pi\tilde{\phi} + \int_{S_0} \tilde{\phi}' \sqrt{1 + |\nabla'\eta'|^2} \frac{\partial}{\partial n'} \frac{1}{r} d\mathbf{X}' \quad (15)$$

where S_0 is the projection of S' on to the horizontal plane, which is the same as in Equation (7). After introducing a new variable $D = \frac{\eta' - \eta}{R}$, the above equation becomes (details could be found in [1, 4])

$$\begin{aligned} \int_{S_0} \frac{V'}{R} d\mathbf{X}' &= 2\pi\tilde{\phi} + \int_{S_0} (\eta' - \eta) \nabla' \tilde{\phi}' \cdot \nabla' \frac{1}{R} d\mathbf{X}' \\ &\quad - \int_{S_0} \tilde{\phi}' \left[\frac{1}{(1 + D^2)^{3/2}} - 1 \right] \nabla' \cdot \left[(\eta' - \eta) \nabla' \frac{1}{R} \right] d\mathbf{X}' \\ &\quad - \int_{S_0} \frac{V'}{R} \left(\frac{1}{\sqrt{1 + D^2}} - 1 \right) d\mathbf{X}' \end{aligned} \quad (16)$$

The velocity V can be split into four parts, i.e., $V = V_1 + V_2 + V_3 + V_4$. Each part is given by

$$V_1 = F^{-1} \{ KF \{ \tilde{\phi} \} \} \quad (17)$$

$$V_2 = -F^{-1} \{ KF \{ \eta V_1 \} \} - \nabla \cdot (\eta \nabla \tilde{\phi}) \quad (18)$$

$$\begin{aligned} V_3 = V_{3,I} &= F^{-1} \left\{ \frac{K}{2\pi} F \left\{ \int_{S_0} \tilde{\phi}' \nabla' \cdot \left[(\eta' - \eta) \nabla' \frac{1}{R} \right] \Gamma_1(D) d\mathbf{X}' \right\} \right\} \\ &= F^{-1} \left\{ \frac{K}{2\pi} F \left\{ \int_{S_0} \tilde{\phi}' \frac{(\eta' - \eta) - \mathbf{R} \cdot \nabla' \eta'}{R^3} \Gamma_1(D) d\mathbf{X}' \right\} \right\} \end{aligned} \quad (19)$$

$$V_4 = F^{-1} \left\{ \frac{K}{2\pi} F \left\{ \int_{S_0} \frac{V'}{R} \left(1 - \frac{1}{\sqrt{1 + D^2}} \right) d\mathbf{X}' \right\} \right\} \quad (20)$$

where

$$\Gamma_1(D) = 1 - \frac{1}{(1 + D^2)^{3/2}} \quad (21)$$

Fructus *et al.* [4] had expanded the expression of V_4 to the 3rd order convolutions, plus a remaining integration term, that is

$$\begin{aligned} V_4 &= V_4^{(1)} + V_{4,I}' \\ &= F^{-1} \left\{ -\frac{K}{2} \left[KF \{ \eta^2 V \} - 2F \left\{ \eta F^{-1} \{ KF \{ \eta V \} \} \right\} + F \left\{ \eta^2 F^{-1} \{ KF \{ V \} \} \right\} \right] \right\} \\ &\quad + F^{-1} \left\{ \frac{K}{2\pi} F \left\{ \int \frac{V'}{R} \Upsilon_1(D) d\mathbf{X}' \right\} \right\} \end{aligned} \quad (22)$$

where

$$Y_1(D) = 1 - \frac{1}{\sqrt{1+D^2}} - \frac{1}{2}D^2 \quad (23)$$

$V_4^{(1)}$ denotes the 3rd order convolutions in the first curly-bracket term and $V_{4,I}'$ represents the remaining integration part in the second curly-bracket term on the right of Equation (22). Note that the determination of V_1 , V_2 and V_3 is explicit while the determination of V_4 is implicit and needs iterations.

During iteration for finding V_4 , the initial value of V_4 is firstly estimated by letting $V = V_1 + V_2$ and assuming

$$Err_B = \frac{\int |V^{Iter} - V^{Iter+1}| d\mathbf{X}}{\int |V^{Iter+1}| d\mathbf{X}} < Tol_B \quad (24)$$

with V^{Iter} and V^{Iter+1} being the values of the velocity V at the two successive iterations.

It is noted here that based on the definition of $D = \frac{\eta' - \eta}{R}$, one obtains that $D \rightarrow \partial\eta/\partial R$ or $|D| \rightarrow |\nabla\eta|$ if $R \rightarrow 0$. Thus D represents the local gradient of waves or wave steepness and reflects their nonlinearity. The maximum of D is determined by $|D|_{max} = |\partial\eta/\partial R|_{max}$, where $|\partial\eta/\partial R|_{max}$ is the maximum gradient of the free surface in the spatial domain and may change with time.

2.3. Numerical implementation

Based on the descriptions in [1, 2, 4], we draw out the flow chart in Figure 1 to illustrate the whole numerical scheme and procedure of the spectral boundary integral method. In this figure, the gradient of the free surface $\nabla\eta$ and the velocity potential $\nabla\tilde{\phi}$ are estimated by Fourier and its inverse transform

$$\nabla\eta = F^{-1}\{iKF\{\eta\}\} \quad \text{and} \quad \nabla\tilde{\phi} = F^{-1}\{iKF\{\tilde{\phi}\}\} \quad (25)$$

It is noted that the most time consuming parts are the boundary integral modules involved in Equation (19) and (22). Our main contributions in this paper lie in developing robust numerical techniques to significantly accelerate the procedure.

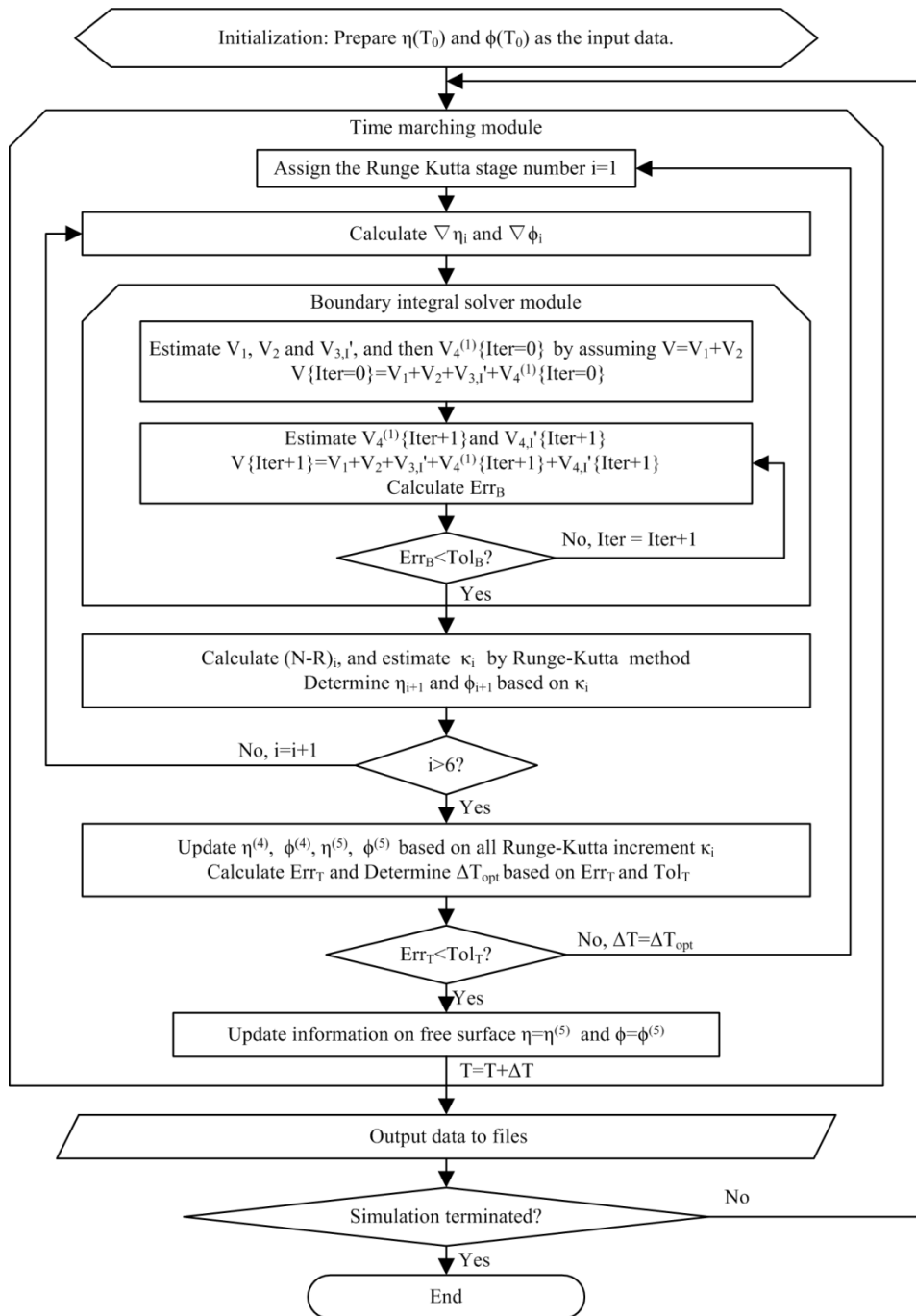


Figure 1. Flow chart for the numerical implementation of Spectral Boundary Integral Method

2.4. Schemes for estimating V_3 and V_4

Fructus *et al.* [4] had expanded the expression of V_4 , and replaced the main part with convolutions to the 3rd order as indicated above. Grue [3] brought the expressions of both V_3 and V_4 to convolutions of the 6th and 7th order respectively. We repeat the expanding procedures and have obtained the equivalent but slightly different results, given by (refer to appendix for details)

$$V_3 = V_{3,C} + V_{3,I} = \underbrace{V_3^{(1)}}_{4th} + \underbrace{V_3^{(2)}}_{6th} + \underbrace{V_{3,I}}_{integration} \tag{26}$$

$$V_4 = V_{4,C} + V_{4,I} = \underbrace{V_4^{(1)}}_{3rd} + \underbrace{V_4^{(2)}}_{5th} + \underbrace{V_4^{(3)}}_{7th} + \underbrace{V_{4,I}}_{integration} \quad (27)$$

$$V_{3,I} = F^{-1} \left\{ \frac{K}{2\pi} F \left\{ \int \tilde{\phi}' \frac{(\eta' - \eta) - \mathbf{R} \cdot \nabla' \eta'}{R^3} \Gamma_2(D) d\mathbf{X}' \right\} \right\} \quad (28)$$

$$V_{4,I} = F^{-1} \left\{ \frac{K}{2\pi} F \left\{ \int \frac{V'}{R} Y_2(D) d\mathbf{X}' \right\} \right\} \quad (29)$$

where

$$\Gamma_2(D) = 1 - \frac{1}{(1 + D^2)^{3/2}} - \frac{3}{2} D^2 + \frac{15}{8} D^4 \quad (30)$$

$$Y_2(D) = 1 - \frac{1}{\sqrt{1 + D^2}} - \frac{1}{2} D^2 + \frac{3}{8} D^4 - \frac{5}{16} D^6 \quad (31)$$

$V_{3,C} = V_3^{(1)} + V_3^{(2)}$ and $V_{4,C} = V_4^{(1)} + V_4^{(2)} + V_4^{(3)}$ are convolution parts and the order of each convolution is labelled at the bottom of each term. The order of the convolution is defined in this way, for example, $F\{V\eta^{l-1}\} \sim O(\varepsilon^l)$, as the l^{th} order, where $\varepsilon = K_0 A$ is the characteristic wave steepness and A is the wave amplitude. When the steepness is small, the order of the integration parts $V_{3,I}$ and $V_{4,I}$ are insignificant compared with the convolution parts, and so can be neglected. Generally, three approaches of estimating V_3 and V_4 are suggested, as summarized in Table I.

Table I. Schemes of the boundary integral solver

Scheme 1	$V_3 = V_{3,I}'$	$V_4 = V_4^{(1)} + V_{4,I}'$
Scheme 2	$V_3 = V_{3,C}$	$V_4 = V_{4,C}$
Scheme 3	$V_3 = V_{3,C} + V_{3,I}$	$V_4 = V_{4,C} + V_{4,I}$

In Scheme 1, V_3 is estimated with integration. V_4 is expanded to 3rd order convolution plus integration term. In Scheme 2, V_3 and V_4 are expanded to the 6th and 7th order convolutions respectively, but ignoring both $V_{3,I}$ and $V_{4,I}$. Scheme 3 is the same as Scheme 2, except the integration parts are included.

It is understood that Scheme 1 and Scheme 3 are equivalent. However, Scheme 3 requires more computational efforts over Scheme 1 on calculating the convolution parts, thus this scheme is only used as benchmark to quantify the difference between Scheme 1 and Scheme 2. In addition, Scheme 2 is the most efficient but is only valid when D is not too big. Assume there exist a critical value D_c , under which the velocity can be solved by Scheme 2; otherwise by Scheme 1, the boundary integral solver module in Figure 1 can be replaced by the flow chart in Figure 2.

It is noted here that the evaluation of integration parts in Schemes 1 and 3 necessitate the computation of the integrals which have a **weakly** singular integrand. This paper will suggest **an improved** numerical technique for evaluating the integrals.

In addition, Fructus *et al.* [4] applied Scheme 1 to Stokes waves while Grue [3] employed Scheme 2 to simulate 3D wave fields, as indicated above. One of main contributions of this paper is to suggest mixing the two schemes together and more importantly to develop a technique for quantitatively determining the critical value D_c , so that the computation can automatically switch to Scheme 1 or Scheme 2 according to the instantaneous value of $|D|_{max}$, significantly accelerating the computation of wave fields. The details about this will be presented in the later section below.

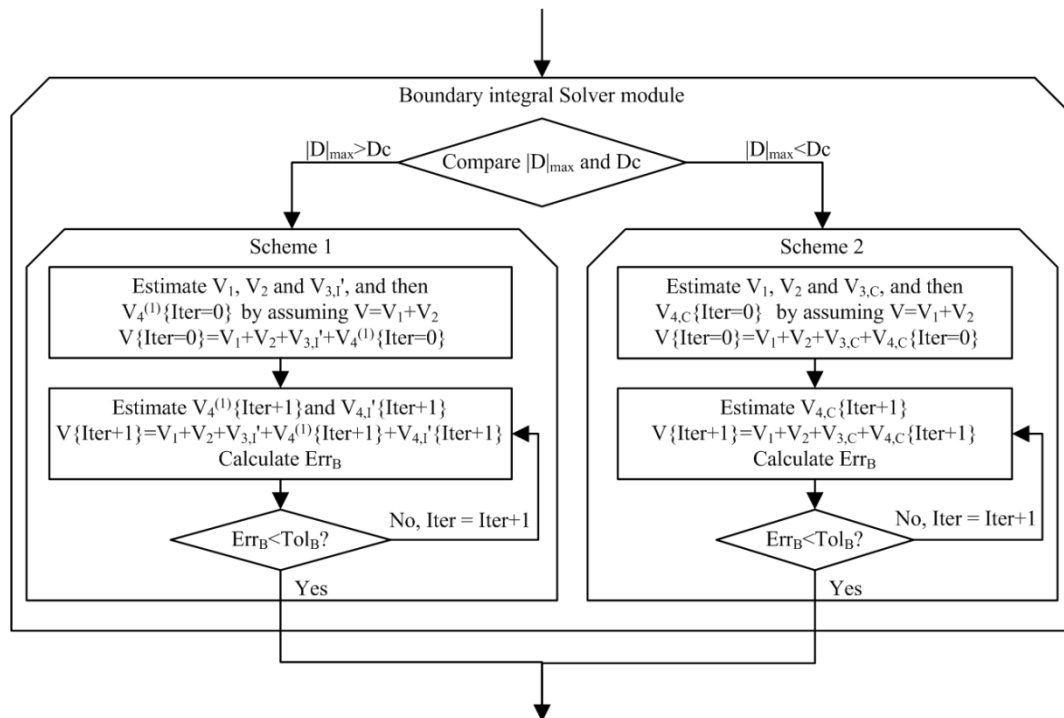


Figure 2. The flow chart of the numerical scheme for solving the boundary integral equation

3. DE-SINGULARITY TECHNIQUE

As mentioned in previous section, the integrals in Equations (19), (22), (28) and (29) have weak singular integrands. Such singularity is an inherited problem for all methods based on the boundary integrals dealing with gravity water waves, from when they were introduced by Longuet-Higgins & Cokelet [18] in their study on the 2D overturning waves. In their paper, the normal velocity ϕ_n appeared in $\int \phi_n \ln s ds$, where s is the arc-length on the boundary, was expanded at $s = 0$ and $s^i \ln s$ was integrated analytically. Grilli *et al.* [19] dealt with the singular integrals by using so called ‘singularity extraction’ method for their normal boundary element method applying to 3D wave problems. In the approach, they introduced the polar coordinates and then transformed the principle integration to a regular integration.

For the Spectral Boundary Integral Method, Fructus *et al.* [4] suggested evaluating the integrands at nodes $\mathbf{X} + \frac{1}{2}\Delta\mathbf{X}$, and shifting back to regular nodes through Fourier interpolation. This method is equivalent to evaluating the integrations without

considering the elements around the singular points so that the contributions to the integration coming from this area are neglected. The smaller of the neglected area is, the more accurate the numerical integration is. In other words, to achieve high accuracy of results, the number of elements splitting the free surface has to be large. This can decelerate the computational process. In this paper, an alternative technique is suggested to evaluate the singular integrals for the the spectral boundary integral method.

3.1. *Weakly singular integral in V_4*

Similar to the strategy by Grilli *et al.* [19], we **re-write** the integration part of V_4 around the singular point as

$$\lim_{\sigma \rightarrow 0} \int_{S-\sigma} \frac{V'Y_i}{R} d\mathbf{X}' = \lim_{\sigma \rightarrow 0} \int_{S-\sigma} \frac{\tilde{f}(\mathbf{X}')}{R} d\mathbf{X}' \quad (32)$$

where Y_i is given by Equation (23) or (31), σ is an area surrounding the singular point. Using the local polar coordinates illustrated in Figure 3, the right hand side of Equation (32) can be rewritten as

$$\begin{aligned} \lim_{\sigma \rightarrow 0} \int_{S-\sigma} \frac{\tilde{f}(\mathbf{X}')}{R} d\mathbf{X}' &= \lim_{\delta \rightarrow 0} \int_0^{2\pi} \int_{\delta}^{\rho(\theta)} f(R, \theta) dR d\theta \\ &= \int_0^{2\pi} \int_0^{\rho(\theta)} f(R, \theta) dR d\theta \end{aligned} \quad (33)$$

where $\rho(\theta)$ and δ are the radius of the area S and σ respectively, and

$$\tilde{f}(\mathbf{X}') = f(R, \theta) = V'Y_i \quad (34)$$

with $D \rightarrow \frac{\partial \eta}{\partial X} \cos \theta + \frac{\partial \eta}{\partial Y} \sin \theta$ for $R \rightarrow 0$. The expression in Equation (34) is not singular $R \rightarrow 0$. For each value of θ from 0 to 2π , one can assume $f(R, \theta)$ vary linearly along R . Thus a two point trapezium rule is enough for evaluation.

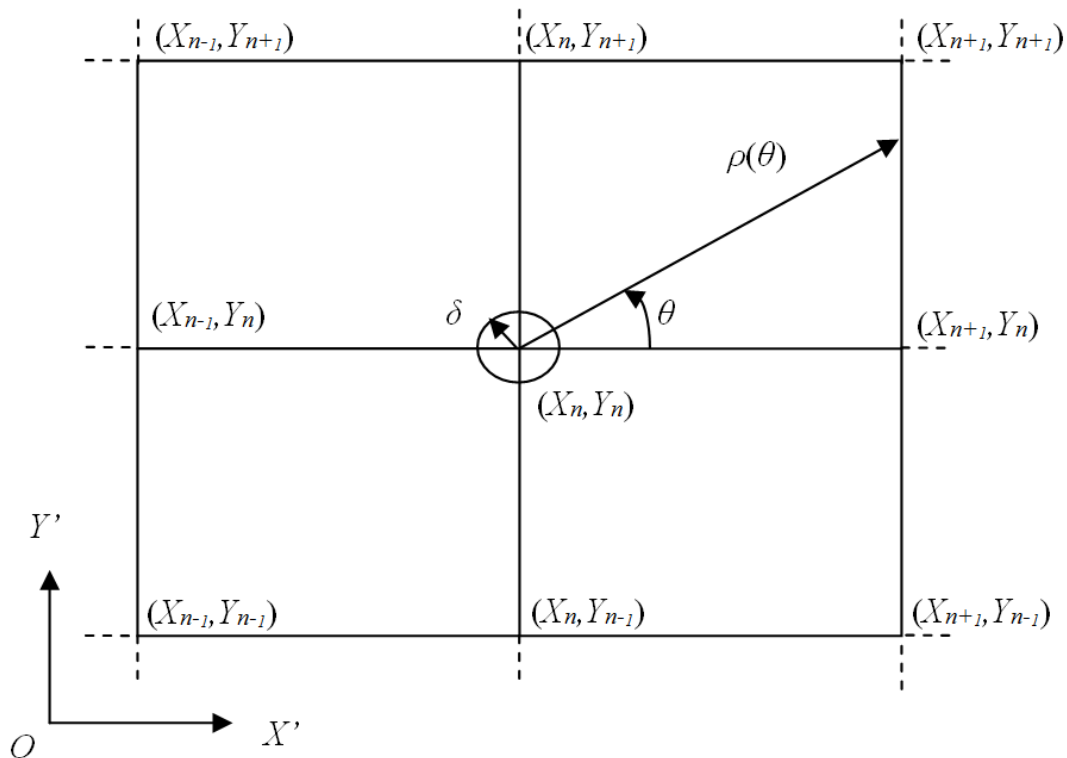


Figure 3. The local polar coordinates for the elements near the singular point

3.2. *Weakly singular integral in V_3*

Following the same strategy, **this weakly** singular integral around the singular point in the expression of V_3 is written as

$$\lim_{\sigma \rightarrow 0} \int_{S-\sigma} \frac{\tilde{g}(\mathbf{X}')}{R^2} d\mathbf{X}' = \lim_{\sigma \rightarrow 0} \int_{S-\sigma} \frac{g(R, \theta)}{R} dR d\theta \quad (35)$$

where

$$g(R, \theta) = \tilde{g}(\mathbf{X}') = \tilde{\phi}' \left(D - \frac{\mathbf{R} \cdot \nabla' \eta'}{R} \right) \Gamma_i \quad (36)$$

and Γ_i is defined by Equation (21) or (30). Note that $\lim_{R \rightarrow 0} \left(\frac{\mathbf{R} \cdot \nabla' \eta'}{R} - D \right) = 0$, which means $g(R=0, \theta) = 0$. Thus, in order to evaluate the integral numerically, we approximate $g(R, \theta)$ with the first order Taylor series

$$g(R, \theta) = g(0, \theta) + \frac{\partial g}{\partial R}(0, \theta) R + O(R^2) \quad (37)$$

Then we have

$$\int_0^{2\pi} \int_0^{\rho(\theta)} \frac{g(R, \theta)}{R} dR d\theta = \int_0^{2\pi} \int_0^{\rho(\theta)} \frac{\partial g}{\partial R}(0, \theta) dR d\theta = \int_0^{2\pi} g(R = \rho, \theta) d\theta \quad (38)$$

which provides a solution for converting the **weakly** singular integration to a regular integration, as there is no singularity in $\frac{\partial g}{\partial R}(0, \theta)$. **To achieve it, the first order**

approximation to $g(R, \theta)$ has been used so that the integration with respect to R leads to $g(R = \rho, \theta)$. The last integral in Eq. (38) is estimated by using one dimensional trapezium rule.

3.3. Effectiveness of the de-singular techniques for evaluating V_3 and V_4

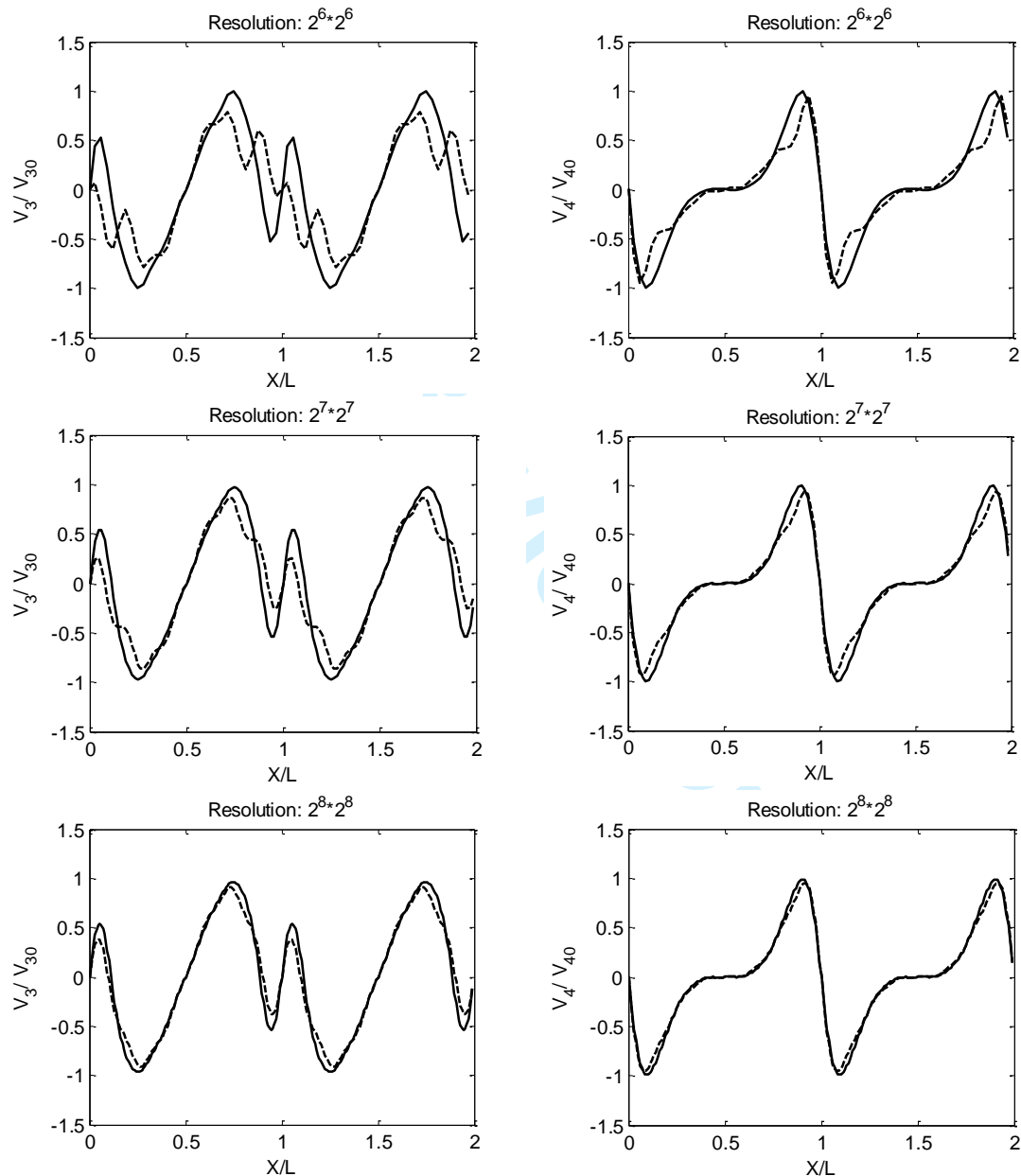
In order to show how effective the above de-singular techniques are, the cases for Stokes waves presented in [4] are tested in this section. To model the case, the initial free surface elevation and velocity potential on the free surface are calculated by using the Fenton's numerical solver [35] up to 7th order with the wave steepness of $\varepsilon = \pi H/L = 0.2985$ (H is the wave height and $L = 2\pi$ is the wave length) in a spatial domain of $2L \times 2L$. In addition, our numerical tests indicate that any value of $Tol_B \leq 1E - 5$ in Equation (24) leads to almost the same results and so the value of Tol_B is taken as $1E - 5$ hereafter.

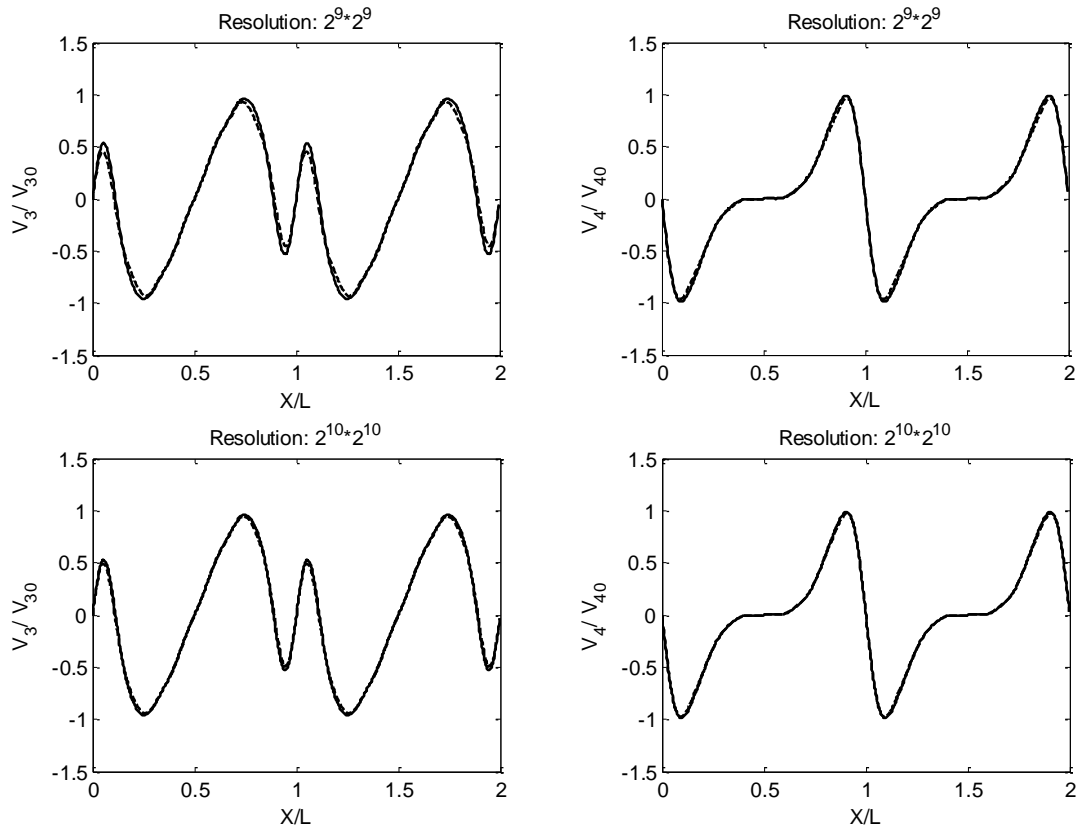
The specific values of V_3 and V_4 are time-dependent. We will first examine the effectiveness of the de-singularity technique using the profiles of V_3 and V_4 at the first time step. These profiles obtained by the methods with or without the de-singularity technique are shown in Figure 4 for different numbers of elements represented by the resolution. The profiles are normalized by V_{30} and V_{40} , which are the maxima of V_3 and V_4 corresponding to the resolution $2^{10} \times 2^{10}$. The results for the case without the de-singularity technique are obtained by using the same method as in [4], that is, the singularity is avoided by evaluating the integrands of V_3 and V_4 at a shifted point $(X + \frac{1}{2}\Delta X)$. As the de-singularity techniques are relevant only to the integration parts in V_3 and V_4 , the results plotted are only these parts in V_3 and V_4 . As can be seen from Figure 4, without the de-singularity technique, the peak values of both V_3 and V_4 are significantly under-estimated when the resolution is not sufficiently high. With increase of the resolution, the profiles of V_3 and V_4 gradually coincide with each other. Specifically, at the resolution of $2^9 \times 2^9$, the difference between them becomes negligible. This demonstrates that the approach proposed in [4] can give accurate results but requires higher resolution. In order to shed more light on the performance of the techniques, their errors are analyzed using the following equations

$$\begin{aligned} Error\{V_3\} &= \frac{\int |V_3 - V_3^{(N=2^{10})}| dX}{\int |V_3^{(N=2^{10})}| dX} \\ Error\{V_4\} &= \frac{\int |V_4 - V_4^{(N=2^{10})}| dX}{\int |V_4^{(N=2^{10})}| dX} \end{aligned} \quad (39)$$

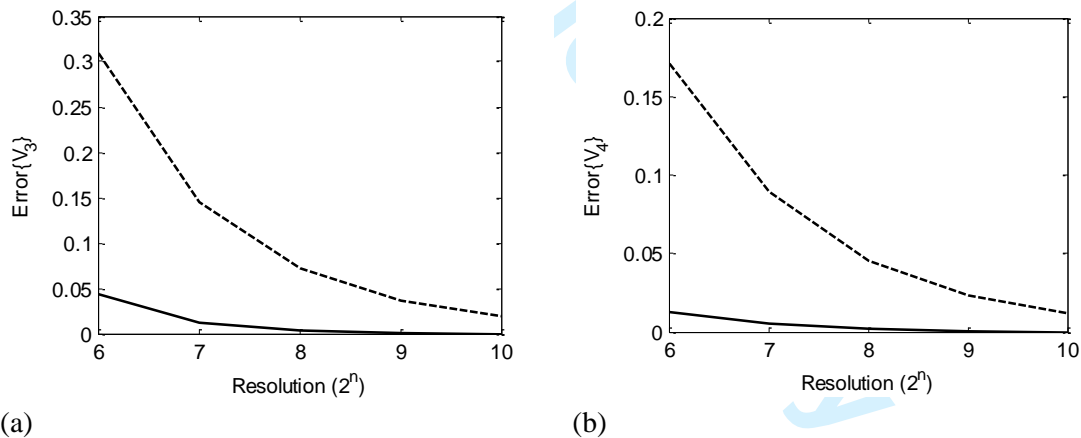
where $V_3^{(N=2^{10})}$ and $V_4^{(N=2^{10})}$ are the values of V_3 and V_4 calculated using resolution of $2^{10} \times 2^{10}$, and the integrations are made over the whole projected free surface. The errors against the different resolutions are shown in Figure 5. It can be seen that the error corresponding to the results obtained by using the de-singularity

technique for the resolution of $2^6 \times 2^6$ is as small as that obtained without the de-singularity technique for the resolution of $2^{10} \times 2^{10}$, while the error from the method without the de-singularity technique for the resolution of $2^6 \times 2^6$ is more than 6 times larger than the latter. This further demonstrates that the de-singularity technique help achieving the similar results with much low resolution or achieving the results with higher accuracy by using the same resolution, compared to the approach suggested in [4], which also leads to exact results but with relatively slower convergent rate.



Figure 4. Profiles of V_3 and V_4

Solid: with de-singularity technique; Dash: without de-singularity technique

Figure 5. Relative error of the profiles of V_3 (a) and V_4 (b)

Solid: with de-singularity technique; Dash: without de-singularity technique

Next, the effects of the de-singularity technique on overall wave propagation of a long period will be examined. The same waves for Figure 4 and Figure 5 are considered but simulated in different sizes ($2L \times 2L$, $4L \times 2L$ and $8L \times 2L$) of the spatial domain. To simulate these cases, the resolution used is $2^6 \times 2^6$, $2^7 \times 2^6$ and $2^8 \times 2^6$, (i.e., the number of elements per wave length is the same), respectively. The wave profiles after the simulation of $1000T_0$ (T_0 is the wave period output by the Fenton's numerical solver [35], which is 6.0095 in this case) are plotted in Figure 6. If there would be no error, the profiles after the propagation of $1000T_0$ should coincide

with the initial profile (the dotted line in the figure). One can see from this figure that the profile obtained without the de-singularity technique has a large phase shift (about 20 degree), while that obtained with the de-singularity technique has only a small phase shift (about 4 degree). The phase shift is gradually accumulated during the simulation. The variation of the phase shift with time is depicted in Figure 7 for different sizes of spatial domain. It clearly shows that the phase shift varies linearly with time and eventual values are almost the same for different domains. In addition, the effects of Tol_T used in Equation (13) are also shown in this figure and in Table II. All the information confirms that $Tol_T = 1E - 7$ is sufficiently small to give consistent results.

Table II. Phase shift with different experimental conditions

Phase shift (degree)	$Tol_T = 1E - 6$			$Tol_T = 1E - 7$			$Tol_T = 1E - 8$		
	o	×	√	o	×	√	o	×	√
$2L \times 2L$ domain	-56	19.52	4.33	16	19.60	4.26	18	19.61	4.25
$4L \times 2L$ domain	-	19.56	4.29	-	19.60	4.25	-	19.61	4.25
$8L \times 2L$ domain	-	19.58	4.26	-	19.61	4.25	-	19.61	4.25

Note: ‘o’ result from Fructus *et al.*[4]; ‘×’ without de-singularity technique; ‘√’ with de-singularity technique

To further examine the effectiveness of the new de-singularity technique quantitatively, the errors defined in two different ways are introduced below:

a) The total phase shift error

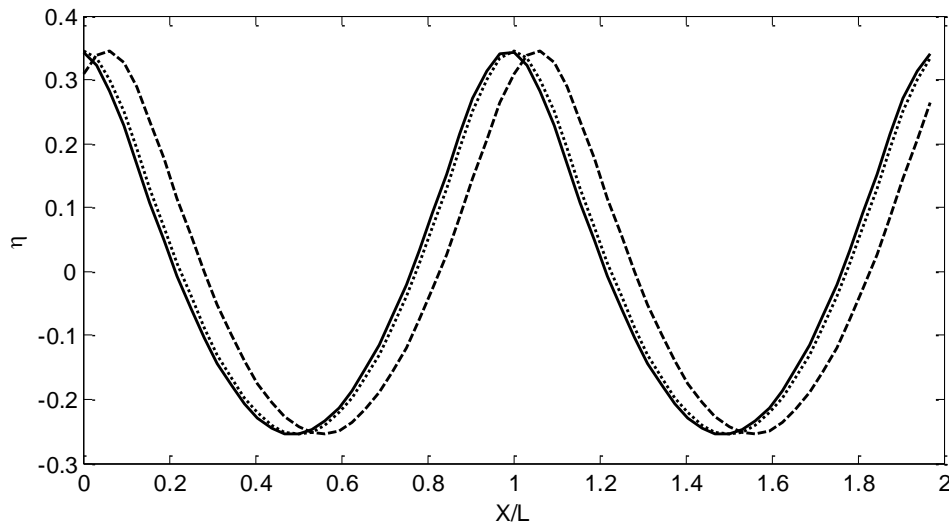
$$Err_1 = 100 \frac{|\Delta\varphi|}{2\pi} \quad (40)$$

b) The mean phase shift error per wave period

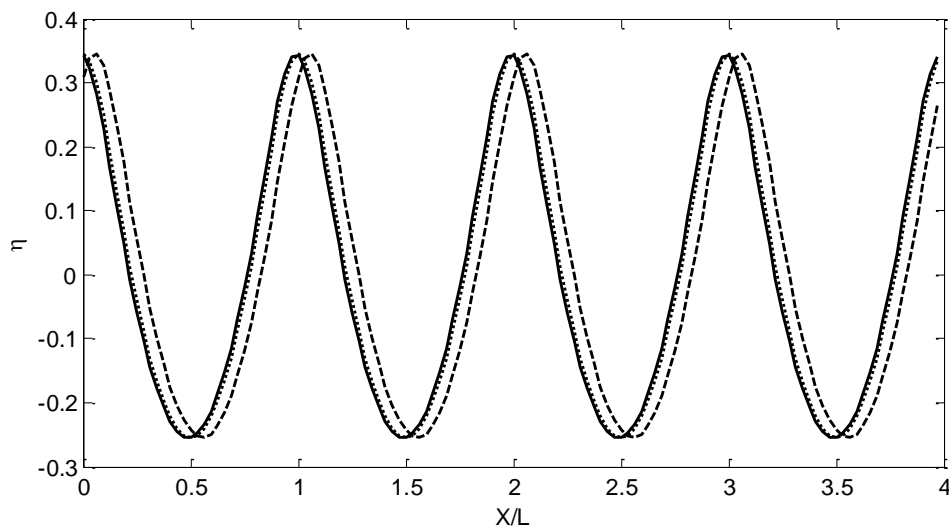
$$Err_2 = \frac{Err_1}{N_{to}} \quad (41)$$

where $\Delta\varphi$ is the total phase shift in radians over the whole period of simulation and N_{to} is the total number of wave periods of simulation, which is 1000 in this case. The errors of the same case as in Figure 6(a) for the domain size of $2L \times 2L$ but obtained using different resolutions are plotted in Figure 8(a), where the number of horizontal axis represents the power (n) of 2^n (the same employed hereafter). In addition, the CPU time against different errors for running all the simulations up to $1000T_0$ on a workstation equipped with the Intel Xeon E5-2630 v2 of 2.6GHz processor are depicted in Figure 8(b). All figures involving the CPU time appears in this paper are based on the same workstation. The results clearly show that for the case with the wave steepness of $\varepsilon = 0.2985$, use of the de-singularity technique allows considerably lower resolution or requires much less CPU time to achieve the same level of accuracy, compared without use of the de-singularity technique. For example, to achieve the results with an error of about 2.5% in terms of Err_1 needs the resolution of $2^5 \times 2^5$ and the CPU time of 2×10^3 seconds with use of the de-singularity technique; otherwise, it needs the resolution of $2^7 \times 2^7$ and the CPU time of about 1×10^4 seconds.

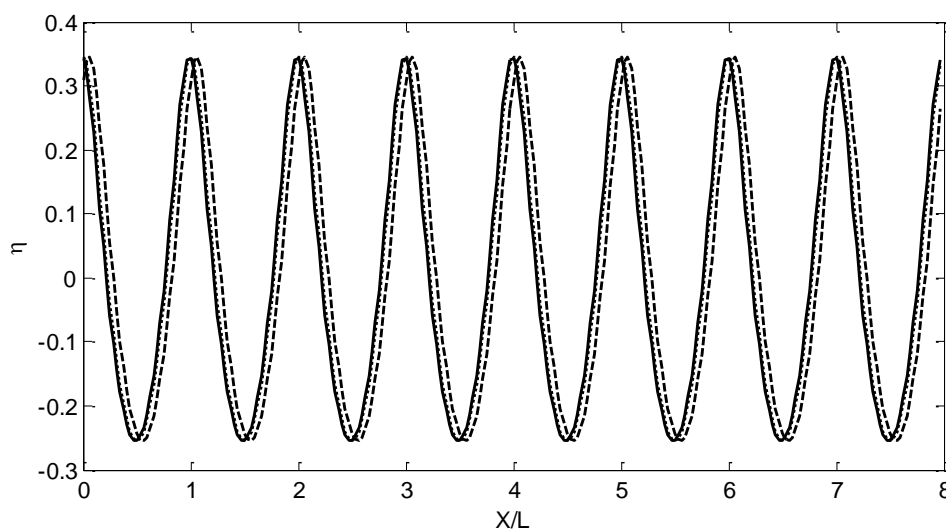
The ratio of the minimum resolutions and corresponding CPU time needed to achieve the error less than 2.5% by the methods with and without use of the de-singularity technique are shown in Figure 9. The ratio in this figure is calculated in the way that the value of the method without the de-singularity technique is divided by that of the method with the de-singularity technique. The figure demonstrates that the minimum resolution and corresponding CPU time used by the two methods with and without the de-singularity technique are almost the same for the cases with small wave steepness. However, for the cases with larger wave steepness (specifically, $\varepsilon \geq 0.2$), the method with use of the de-singularity technique needs much less resolution and CPU time than the one without use of the de-singularity technique. For example, for the case of $\varepsilon = 0.36$, the CPU time required by the method with use of the de-singularity technique is only 1% of that without it to yield the results at the said error level. All the above information evidences that the de-singularity technique is particularly effective for modelling strong nonlinear waves in terms of the resolution and so the CPU time required.



(a) Domain size: $2L \times 2L$



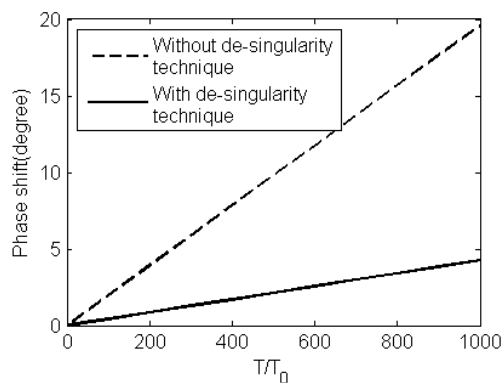
(b) Domain size: $4L \times 2L$



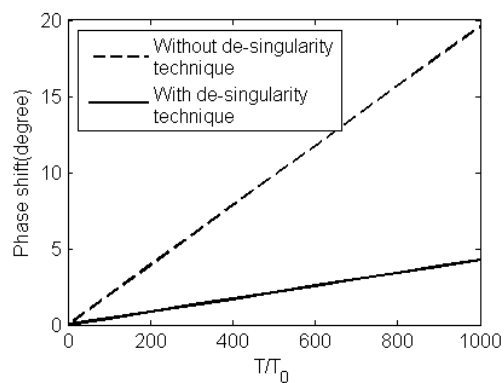
(c) Domain size: $8L \times 2L$

Figure 6. Profiles of the free surfaces

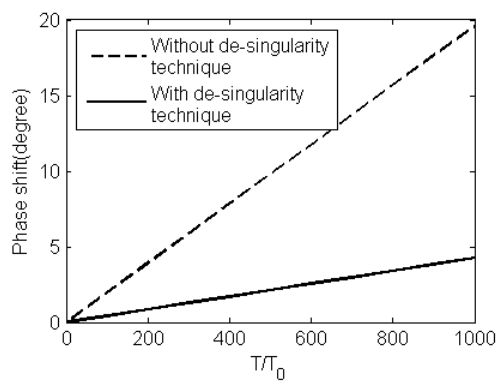
Dot: at initial moment; Dash: after simulation of $1000T_0$ without de-singularity technique;
Solid: after simulation of $1000T_0$ with de-singularity technique



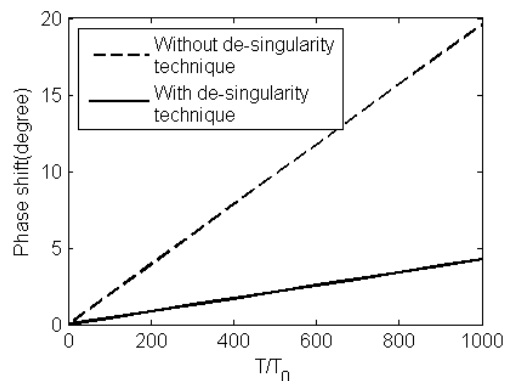
(a)



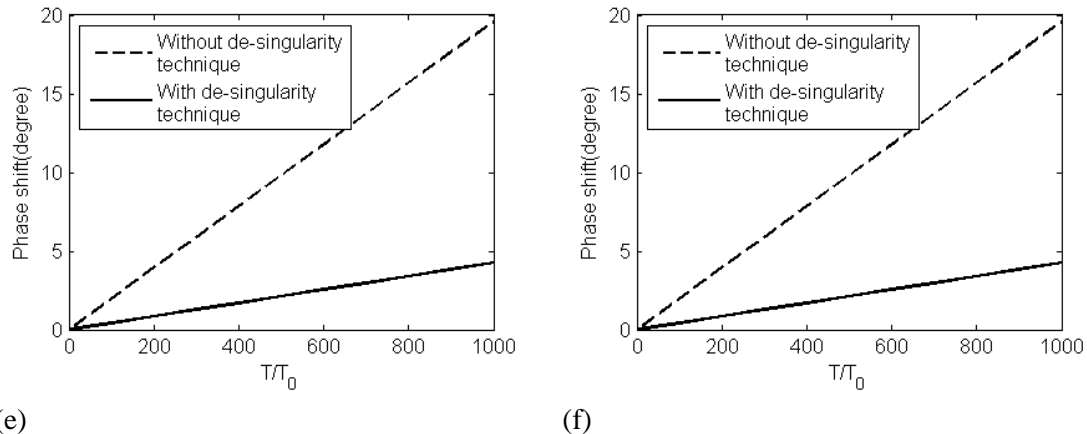
(b)



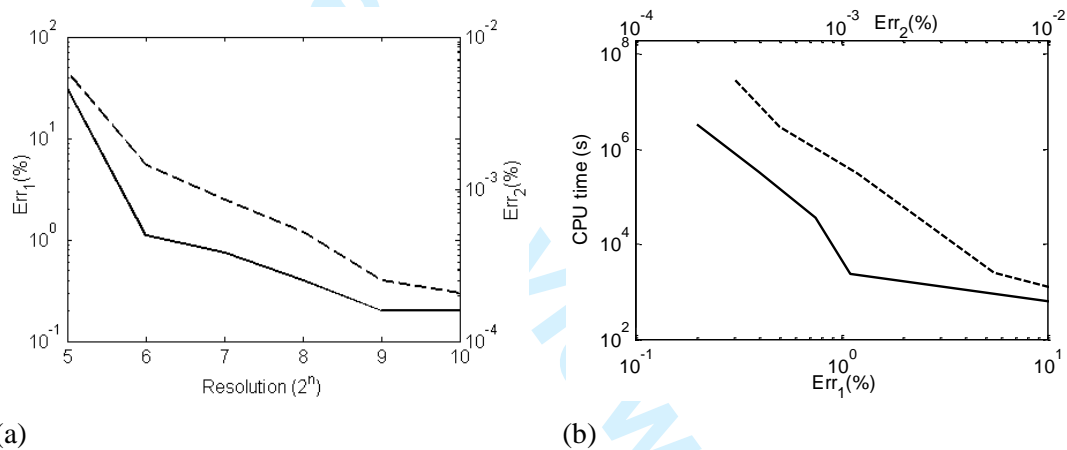
(c)



(d)

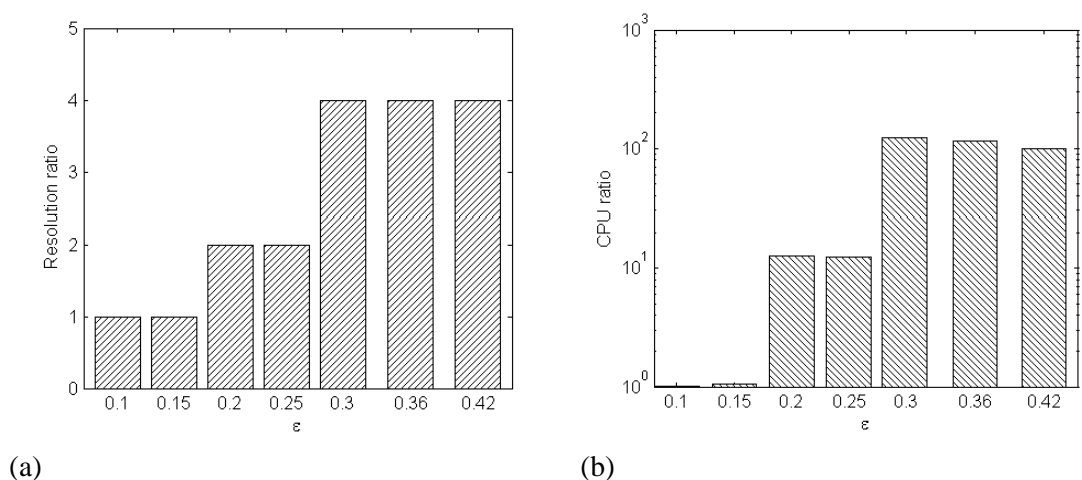


(e) (f)
 Figure 7. Variation of the phase shift of wave profiles with time (a) in a domain of $2L \times 2L$, $Tol_T = 1E - 7$; (b) in a domain of $2L \times 2L$, $Tol_T = 1E - 8$; (c) in a domain of $4L \times 2L$, $Tol_T = 1E - 7$; (d) in a domain of $4L \times 2L$, $Tol_T = 1E - 8$; (e) in a domain of $8L \times 2L$ waves, $Tol_T = 1E - 7$; (f) in a domain of $8L \times 2L$, $Tol_T = 1E - 8$



(a) (b)
 Figure 8. Error against resolution (a) and CPU time against Error (b) for the case with a domain of $2L \times 2L$ and $\epsilon = 0.2985$.

Solid: with de-singularity technique; Dash: without de-singularity technique



(a) (b)
 Figure 9. Resolution (a) and CPU time ratio (b) to achieve $Err_1 < 2.5\%$ for different values of steepness (Ratio = value of the method without the de-singularity technique /value of the

method with the de-singularity technique)

4. TECHNIQUES FOR ANTI-ALIASING (TAA)

In addition to the integration parts discussed in the previous section, one needs to numerically calculate the convolution parts in the spectral method. For this purpose, the discrete Fast Fourier Transform (FFT) or its inverse transform is repeatedly performed on a limited number of N points. As well documented (e.g. [36]), the calculation of the convolutions (particularly the higher order ones involving more than two functions, like V_3 and V_4 in Section 2) in this way suffers aliasing errors when improper resolution is used [36]. The aliasing errors may be theoretically eliminated by using sufficiently high resolution to ensure that the wave component corresponding to the highest frequency or wave number is correctly sampled. However, use of high resolution requires high computational costs. Added to this, it is difficult to predict the highest frequency during the simulation of nonlinear waves because the components of higher frequency are continuously evolving during the simulation due to nonlinearity. Therefore, anti-aliasing techniques are necessary to model nonlinear water waves. As discussed in [36], there are largely two types of anti-aliasing techniques for general fluid problems: one based on truncation (or padding) and the other based on phase shifting.

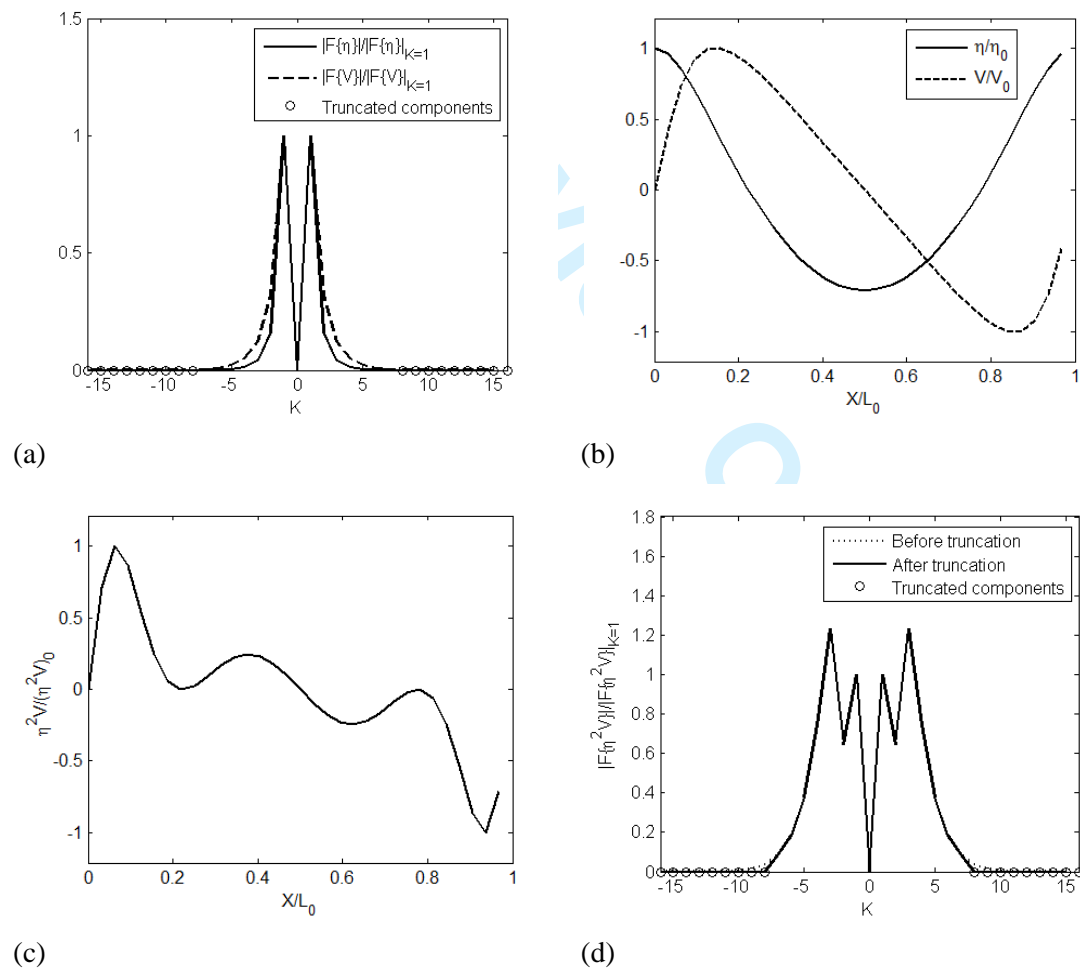
In the research for modelling nonlinear water waves, Dommermuth & Yue [31] dealt with the pseudo-spectral product involving two terms by doubling the width of the spectrum of each term and multiplying in physical domain. Then the spectrum of this product is truncated to the original width after applying Fourier transform. For products involving two or more terms, the multiplication is done successively where each factor is made aliasing-free before multiplied by the next term. Nicholls [32] and Xu & Guyenne [37] introduced a filter to remove the aliased components for $|K| > \nu|K|_{max}$ in spectrum domain, where ν is determined by the method consistent with [36]. Clamond & Grue [1] approximated the 3rd order convolution by doubling the spectra in order to remove the aliasing errors (4-half rule). All the techniques used in the cited papers are based on the truncation (or padding) technique. That is perhaps because the technique by using truncation (or padding) is more computationally efficient than that by using phase shifting. Three techniques will be discussed below. All of them are formed by using truncation (or padding).

For the illustration purpose to aid our discussions below, Stokes wave with $\varepsilon = 0.2985$ similar to that Figure 6 but within a domain of $L \times L$ will be used. Other parameters will be given when necessary. Suppose the resolution of the surface elevation and velocity potential for FFT is N , and the width of their spectrum will be $-N/2 \sim N/2$. In many figures below, the spectra are divided by the Fourier coefficient of $K = 1$, and the quantities in the physical domain is normalized by its maxima.

4.1. Anti-aliasing Techniques

TAA1: (2/(I+1)-rule). The spectrum width of the I^{th} order convolution will be truncated to $N/(I + 1)$. This follows exactly the zero-padding method in [36]. For

example, in order to estimate $F\{\eta^2V\}$, which is a part $V_4^{(1)}$ and is the 3rd order convolution, the spectrum of η and V will be truncated to $-32/4 \sim 32/4$ from the range of $-32/2 \sim 32/2$ as shown in Figure 10(a) for $N = 32$, where the points circled out are padded as zero. Then the product of η^2V is calculated in the physical spatial domain after applying inverse Fourier transform to give both η and V , as shown in Figure 10(b) and (c). At last, the product of η^2V is transformed back to spectral space and their spectra $F\{\eta^2V\}$ are truncated to $-32/4 \sim 32/4$, which is illustrated in Figure 10(d). Similarly, to estimate $F\{V\eta^6\}$, which is a part of $V_4^{(3)}$ and is the 7th order convolution. The spectra of η and V are truncated to $-32/8 \sim 32/8$ before calculating $V\eta^6$, as shown in Figure 10(e). After the multiplication of the functions in physical space (Figure 10(f) and (g)), the spectrum $F\{V\eta^6\}$ is truncated to $-32/8 \sim 32/8$ (Figure 10(h)).



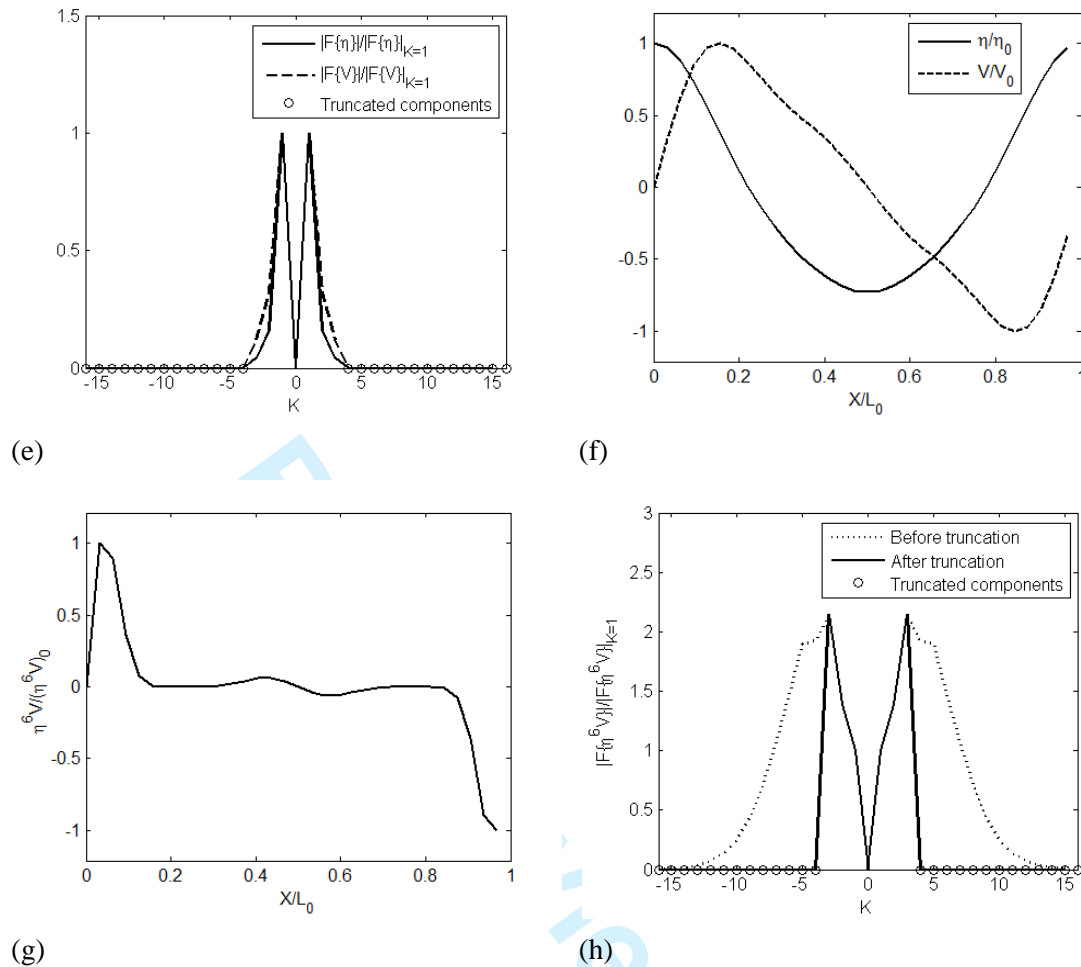


Figure 10. Illustration of TAA1

TAA2: (Repeated 2/4-rule). This technique was suggested and referred as repeated 4-half rule by Clamond & Grue [1] and Fructus *et al.* [4]. The spectrum width of convolutions of the 2nd and 3rd order are truncated to $-N/4 \sim N/4$. Convolutions of 4th order and higher will be estimated using a repeated 2/4-rule, in which the convolution is broken down into several terms, each one being of lower than the 3rd order. Each individual term is estimated with 2/4-rule. For example, $F\{\eta^3 \nabla \tilde{\phi}\}$ is firstly split into $F\{\eta^3\} * F\{\nabla \tilde{\phi}\}$. Applying the 2/4-rule (same as in TAA1) gives η^3 and $\nabla \tilde{\phi}$ separately (Figure 11(a) – (d) and then $\eta^3 \nabla \tilde{\phi}$ (Figure 11(e)) in the physical space. After that, $F\{\eta^3 \nabla \tilde{\phi}\}$ is computed by FFT and its spectrum is truncated to $-N/4 \sim N/4$, as shown in Figure 11(f).

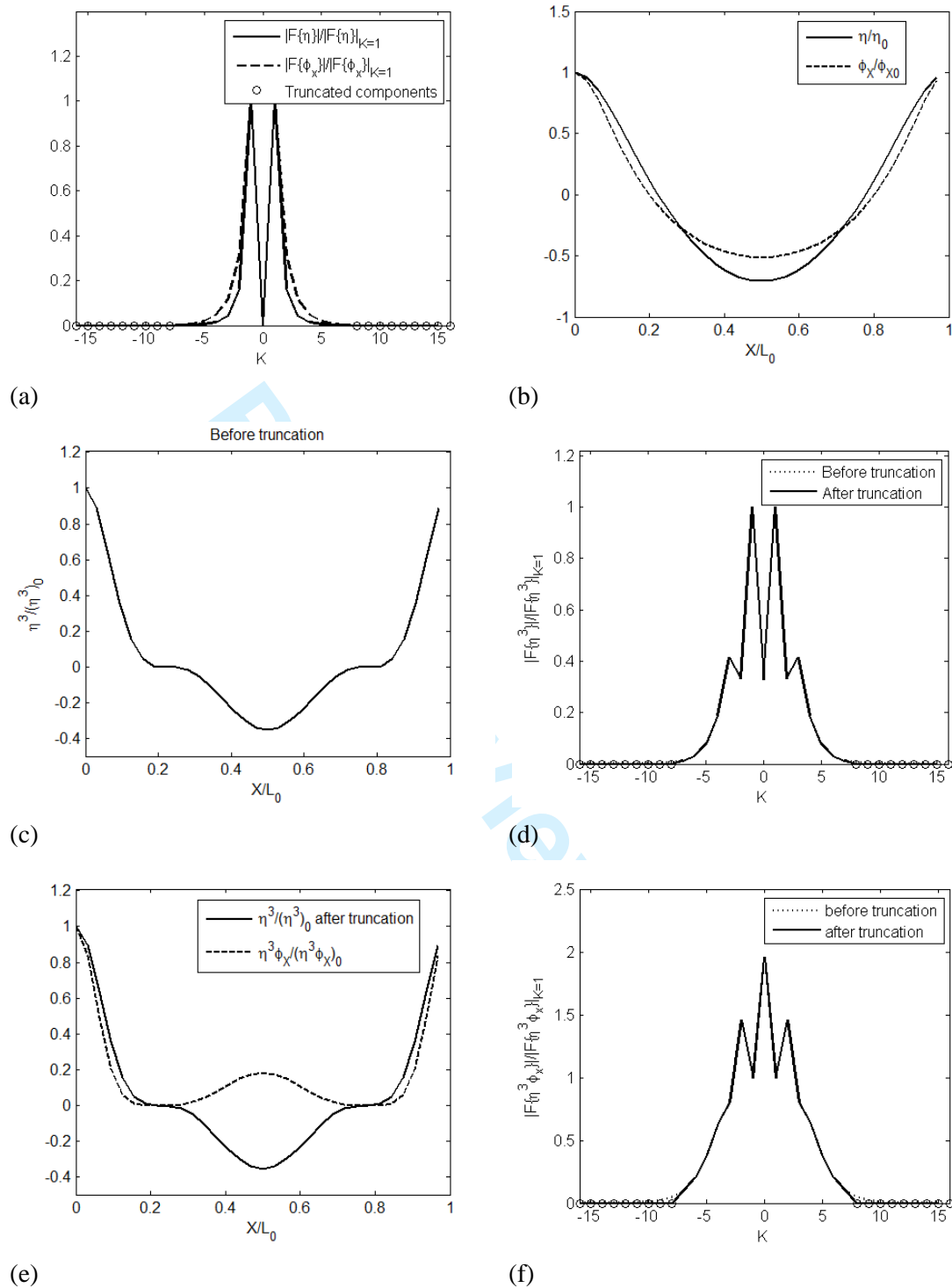


Figure 11. Illustration of TAA2

Although this technique may work in some cases, it is found not to be accurate generally. For example, when the technique is applied to evaluate $V_4^{(2)}$ (Appendix) of 5th order convolution for a Stokes wave of $\varepsilon = 0.3$ in a domain of one wave length at the resolution of 2^5 , the result in Figure 12 is obtained, where the solid line is the result obtained by using very high resolution (2^9) for which there should be no

aliasing error. It can be seen that TAA2 give incorrect approximation to $V_4^{(2)}$ at this resolution.

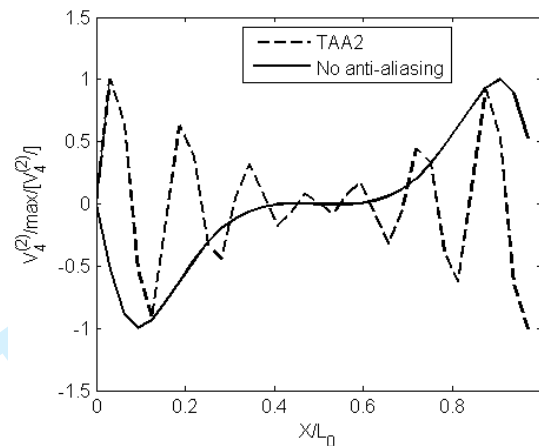


Figure 12. Profiles of $V_4^{(2)}$

TAA3: (Mixed 2/4-2/8-rule). This is a new technique suggested in this paper. For this technique, the convolutions of the 2nd and 3rd order are estimated using the 2/4-rule as in TAA1 and TAA2. The difference lies in dealing with the convolutions of 4th and higher order. To deal with these higher order convolutions, the spectrum of an individual function is padded as zero in the ranges of $-N \sim -N/4$ and $N/4 \sim N$, and then they are inversed to the physical domain. The products of the functions are found before transformed into spectral space. The resulting spectrum is truncated to $-N/4 \sim N/4$ at last. For instance, to estimate $F\{V\eta^6\}$, the spectrum of V and η is padded as zero except for the range of $-32/4 \sim 32/4$ within $-32 \sim 32$ as shown in Figure 13(a) and (b) for $N = 32$ before they are inversed to physical space (Figure 13(c)). Then their product (Figure 13(d)) is computed before transforming it to spectral space (Figure 13(e)). In the spectral space, the spectrum $F\{V\eta^6\}$ is truncated to $-32/4 \sim 32/4$ with all other points padded as zero. As this spectrum is truncated from the range of $-32 \sim 32$ to the range of $-32/4 \sim 32/4$, it actually follows the 2/8-rule. The principle dealing with the higher order convolutions are similar to that of TAA1 but there are some differences: (1) the spectrum of an individual function covers the range of $-N \sim N$ in this technique rather than $-N/2 \sim N/2$ in TAA1; (2) the range of spectrum for all high order (4th and higher) convolutions is the same but it is different for different order in TAA1 and (3) the nonzero width of the last spectrum is generally larger in TAA3 than in TAA1, which can be found by comparing Figure 10(h) with Figure 13(f).

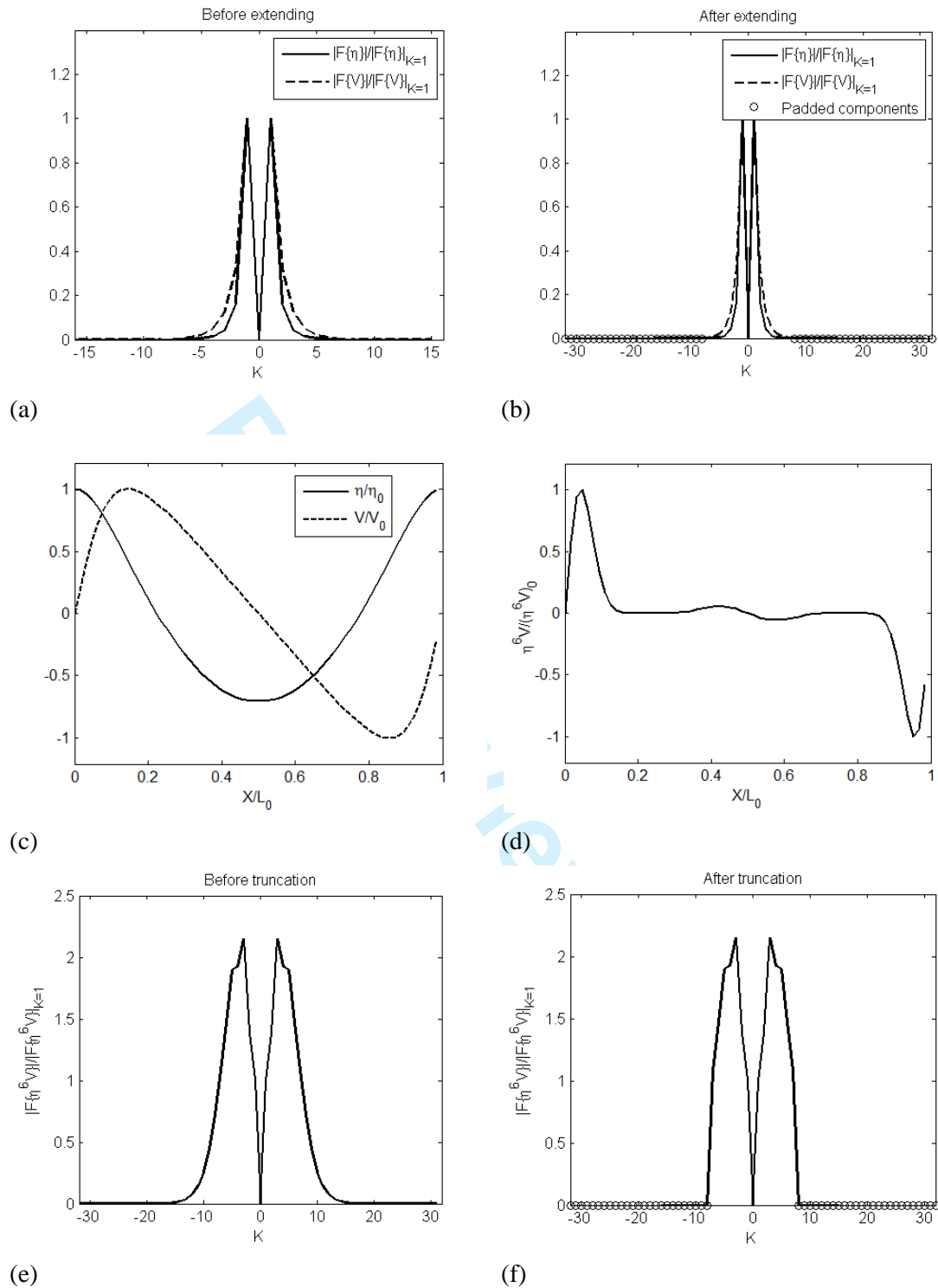


Figure 13. Illustration of TAA3

4.2. Preliminary comparisons of different anti-aliasing techniques

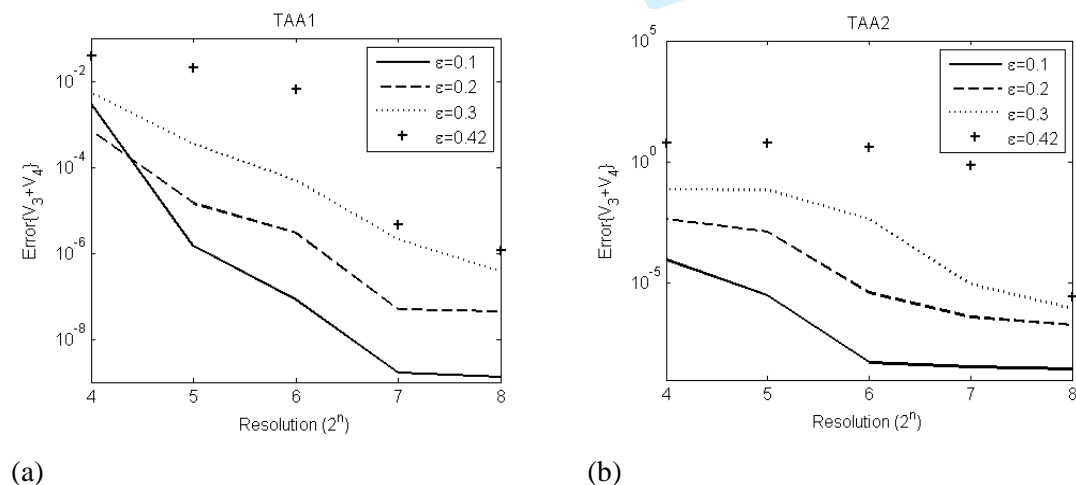
In order to show which one of three anti-aliasing techniques yields better results, preliminary comparative studies have been carried out and some results are presented and discussed in this sub-section. More comparison will be given in later sections. For this purpose, the convolution parts of V_3 and V_4 for the Stokes waves of different wave steepness within a domain of $L \times L$ at the first time step will be evaluated

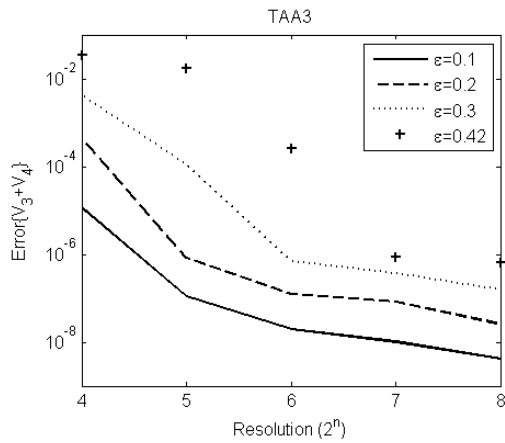
using the above three anti-aliasing techniques and their results will be compared. The aliasing error will be estimated by

$$\text{Error}\{V_3 + V_4\} = \frac{\int \left(\left| V_{3,C}^{(N=2^n)} - V_{3,C}^{(N=2^9)} \right| + \left| V_{4,C}^{(N=2^n)} - V_{4,C}^{(N=2^9)} \right| \right) d\mathbf{X}}{\int |V| d\mathbf{X}} \quad (42)$$

where $V_{3,C}^{(N=2^n)}$ and $V_{4,C}^{(N=2^n)}$ are the convolution parts of V_3 and V_4 with resolution of $2^n * 2^n$ estimated by using one of three anti-aliasing techniques. $V_{3,C}^{(N=2^9)}$ and $V_{4,C}^{(N=2^9)}$ are the convolution parts of V_3 and V_4 computed by using a resolution of $2^9 * 2^9$, which is tested to be the resolution to eliminate the aliasing error without use of any anti-aliasing technique. The aliasing errors corresponding to three methods are plotted in Figure 14. It can be seen that the aliasing errors decrease with increase of resolution but they are larger for larger steepness. The TAA3 clearly over-performs relative to the other two techniques for stronger nonlinear waves, such as these with $\varepsilon = 0.3$ and 0.42 . In these cases, the error of TAA3 is less than $1\text{E-}6$ at the resolution of $2^6 * 2^6$ but the errors of other two is larger than $1\text{E-}6$ at the resolution.

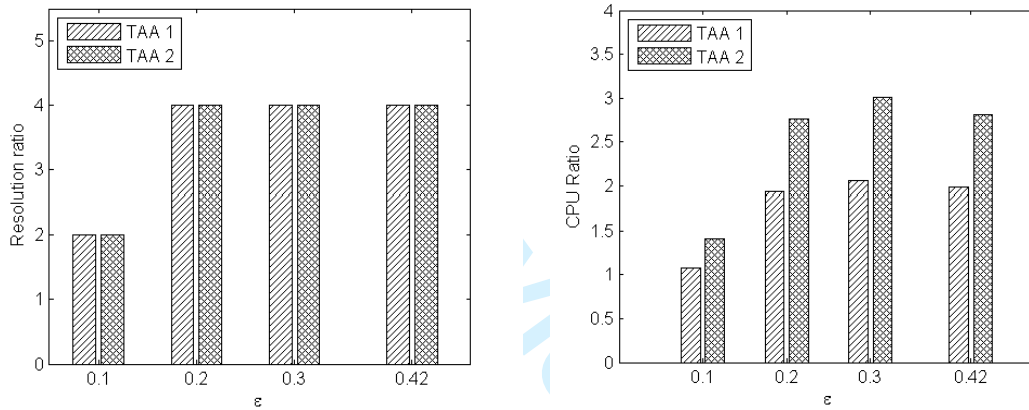
To further demonstrate the fact, Figure 15(a) presents the minimum resolution required to achieve the results with error less than $1\text{E-}6$ by the three different techniques. For the same purpose, Figure 15(b) gives the ratio of CPU time corresponding to the three techniques for evaluating the convolution parts of V_3 and V_4 in one time step. The ratio is estimated by dividing the CPU time of each technique by the CPU time of TAA3. The results clearly indicate that the TAA3 is superior to the others in suppressing the aliasing errors, in particular in estimating the higher order convolutions.





(c)

Figure 14. Aliasing error against different resolutions for different steepness TAA1 (a), TAA2 (b) and TAA3 (c)



(a)

(b)

Figure 15. Resolution (a) and CPU ratio (b) to achieve $Error\{V_3 + V_4\} < 1E - 6$ for different values of steepness (Ratio = value of the method with TAA1 or TAA2 /value of the method with TAA3)

5. TECHNIQUE FOR DETERMINING THE CRITICAL VALUE D_c

As indicated in Table I, one may use one of three schemes to evaluate the velocity V . Fructus *et al.* [4] used the Scheme 1 while Grue [3] employed Scheme 2 with excluding the estimation of the integral parts. Although more convolution terms need to be evaluated in Scheme 2 than Scheme 1, Scheme 2 is expected to be much more efficient as there is no need of evaluating integral parts. To demonstrate this, the ratio of CPU time taken by Scheme 1 to that of Scheme 2 is plotted in Figure 16. The results in this figure are obtained by using the two schemes to model the similar waves in Figure 6 up to a time of $1000T_0$ in a domain of $2L * 2L$ for different steepness. The resolution is selected such that $Err_1 < 2.5\%$. One can see that Scheme 2 is more than 100 time faster when $\epsilon \geq 0.25$. It is noted that the numerical results show that $|D|_{max} < 0.5$ for $\epsilon \leq 0.42$ in the cases associated with Figure 16. In other words, one can just use Scheme 2 to achieve satisfactory results for cases like these.

However, it is not always true. This can be understood from the fact that Scheme 2 is derived from Scheme 1 by expanding V_3 and V_4 up to the 7th order (ε^7) as shown in Appendix. Based on this, Scheme 2 should be only accurate when the maximum gradient of the free surface is less than a critical value D_c . So far, such a critical value has not been quantified, which will be discussed in the following sections.

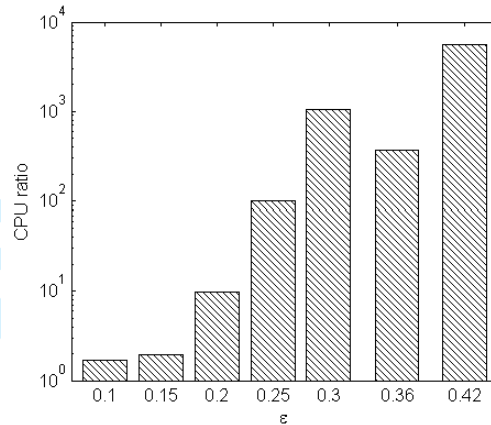


Figure 16. Ratio of CPU time taken by Scheme 1 to that of Scheme 2 for $Err_1 < 2.5\%$

5.1. Estimation of magnitude of D_c

As has been noted in section 2.1, D represents the local gradient of waves and thus its maximum should have a similar order to the wave steepness ε if the wave does not reach the overturning point. In order to estimate the magnitude of D_c , we may assume that $|D|_{max} \approx \varepsilon$. In addition, the magnitude of D_c must be related to the highest order of differences between Scheme 2 and Scheme 3 or Scheme 1. From Table I, the differences come from ignoring $V_{3,I}$ and $V_{4,I}$. From Equation (26) and (27), the leading order of $V_{3,I}$ and $V_{4,I}$ are $O(\varepsilon^8)$ and $O(\varepsilon^9)$ respectively. As the former is one order higher than the latter, the magnitude of D_c may be estimated by using only $V_{3,I}$. To give more specific information about the order of $V_{3,I}$, it has been expanded in Appendix to

$$V_{3,I} = V_3^{(3)} + O(\varepsilon^{10}) \quad (43)$$

where $V_3^{(3)}$ is given in Equation A. 8. To be more specific, let us consider a simple wave described by $\eta = \varepsilon \cos X$ and $\tilde{\phi} = \varepsilon \sin X$, for which $V = \varepsilon \sin X$. For this wave, one obtains, as shown in Equation A. 9,

$$O(V_{3,I}) \sim O(V_3^{(3)}) \sim \frac{69}{2560} \varepsilon^8 \sin(2X) \quad (44)$$

Thus

$$O\left(\frac{V_{3,I}}{V}\right) \sim \frac{69}{2560} \varepsilon^7 \quad (45)$$

Generally, the error due to ignoring the $V_{3,I}$ and $V_{4,I}$ may be estimated by

$$Error_1\{V\} = \frac{\max|V_3^{(3)}|}{\max|V|} \quad (46)$$

It is clear that the order of $Error_1\{V\}$ is $O(\varepsilon^7)$. For the simple wave, it follows that

$$Error_2\{V\} \sim \frac{69}{2560} \varepsilon^8 = \frac{69}{2560} \varepsilon^7 \approx \frac{69}{2560} |D|_{max}^7 \quad (47)$$

5.2. Values of D_c determined by numerical tests

In this subsection, tests will be carried out to further quantify the critical value D_c . To do so, the error of Scheme 2 is estimated by

$$Error_3\{V\} = \frac{\int |V^{(scheme\ 2)} - V^{(scheme\ 3)}| dX}{\int |V^{(scheme\ 3)}| dX} \quad (48)$$

where $V^{(scheme\ 3)}$ is the profile of the velocity V calculated by using Scheme 3 at an instant, which takes into account of all the terms, and $V^{(scheme\ 2)}$ is the profile of velocity V computed by Scheme 2 at the corresponding instant excluding the integral parts. The simulation is first carried out by using Scheme 3, and the data of V , $\tilde{\phi}$ and η at all time steps are saved in files. From these data, $|D|_{max}$ is computed for every time step. Then Scheme 2 is employed to estimate the error in Equation (48), corresponding to the value of $|D|_{max}$ at each time step. Using the information, one can find the critical value D_c for a specified error. The results for three cases will be presented below.

The first case is about a Stokes wave steepened by a moving pressure on the surface. The initial wave of $\varepsilon = 0.15$ is obtained in the same way as for Figure 6. The domain covers one wave length ($L \times L$) and is resolved by $2^7 * 2^7$ points. The duration of the simulation is 5 wave periods (T_0). The pressure distribution on the free surface is specified as

$$p(X, T) = \begin{cases} -p_0 \sin(2\pi T/T_0) \sin(X - CT) & , 0 \leq T \leq T_0/2 \\ 0 & , T > T_0/2 \end{cases} \quad (49)$$

where $p_0 = 0.25$ is the amplitude of the pressure and $C = L/T_0$ is the wave phase speed. The wave profiles at some time steps ($T/T_0 = 0.1, 0.4$ and 0.88) obtained by Scheme 3 are shown in Figure 17(a). It demonstrates that the free surface elevation gradually becomes steeper and steeper. The errors in Equations (46), (47) and (48) corresponding to the values of $|D|_{max}$ are presented in Figure 17(b). It shows that the errors estimated for Scheme 2 using Equations (46) and (48) is less than $2E-4$ and does not increase significantly when $|D|_{max} \leq 0.5$, while it grows exponentially when $|D|_{max}$ exceeds 0.5. In addition, the errors of Scheme 2 have the same trend as the expression of $\frac{69}{2560} |D|_{max}^7$ in Equation (47). Furthermore, the errors estimated by using Equation (46) are closely correlated with these of Equation (48).

To further show this, the similar results for $p_0 = 0.22$ and 0.3 are given in Figure 18(a) and (b), which are consistent with the observation in Figure 17.

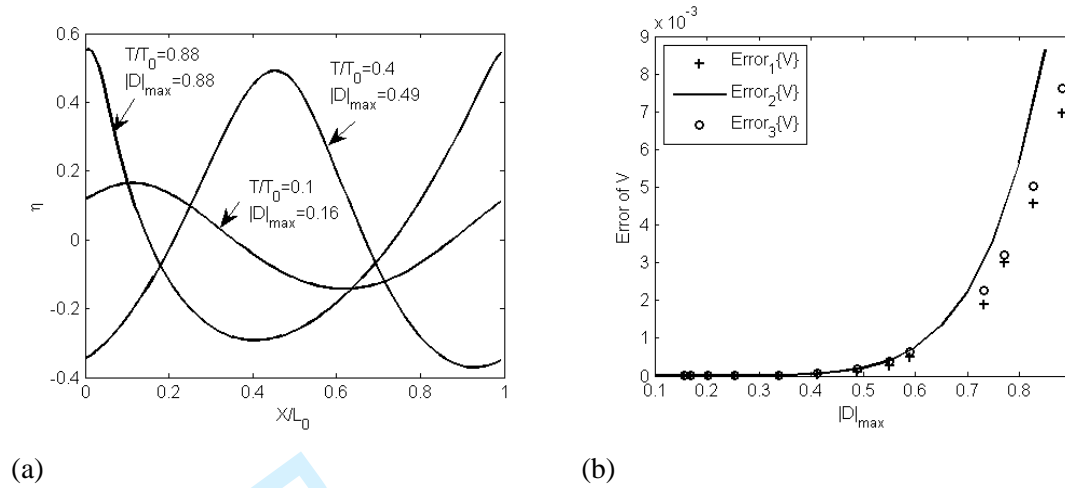


Figure 17. Wave profiles at different instants (a) and numerical error against maximum gradient (b) for $p_0 = 0.25$

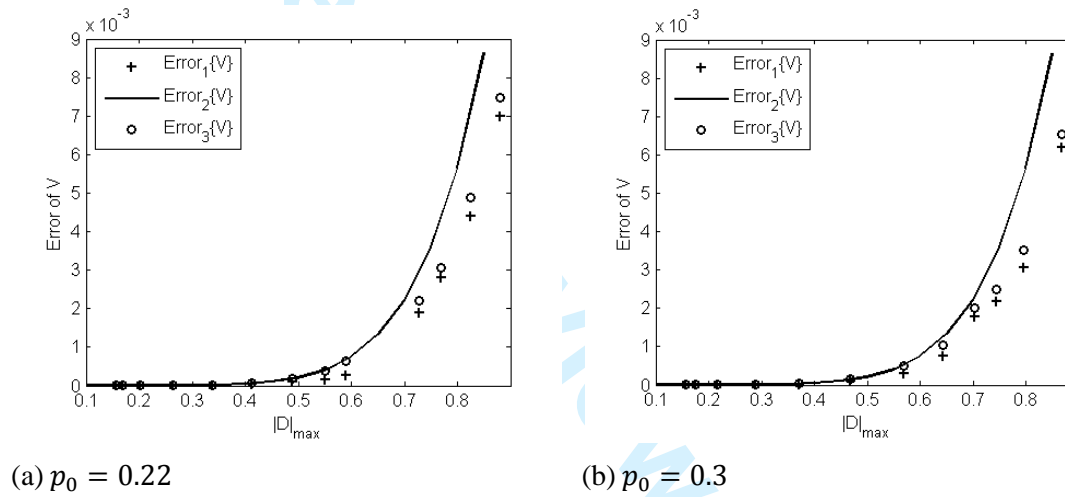
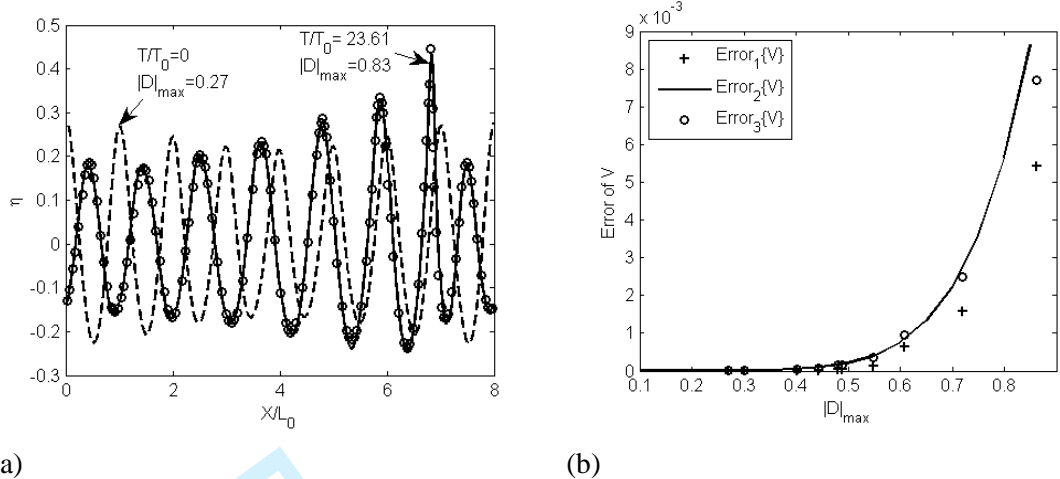


Figure 18. Numerical error against maximum gradient for different pressure amplitude

The second case tested is related to a 2D Benjamin-Feir instability [11]. To do this test, the wave with $\epsilon = 0.22$ generated as in Figure 6 is disturbed by

$$\delta\eta = 0.105\epsilon\cos\left(\frac{9}{8}X - \frac{\pi}{4}\right) + 0.105\epsilon\cos\left(\frac{7}{8}X - \frac{\pi}{4}\right) \tag{50}$$

The domain covers $8L \times L$ which is resolved by $2^{10} \times 2^7$ points. The duration of the simulation is about 30 wave periods. All the setup parameters are the same as in [1]. The free surface profiles at $T/T_0 = 0$ and $T/T_0 = 23.61$ obtained by Scheme 3 are shown in Figure 19(a). The profile at $T/T_0 = 23.61$ from [1], denoted by small circles, is also given and has a little visible difference from that calculated by the method of this paper. The errors of Scheme 2 estimated using Equation (48) are less than $2E-4$ without significant increase when $|D|_{max} \leq 0.5$, while they grow exponentially when $|D|_{max}$ exceeds 0.5 and agrees quite well with that given by Equations (46) and (47).

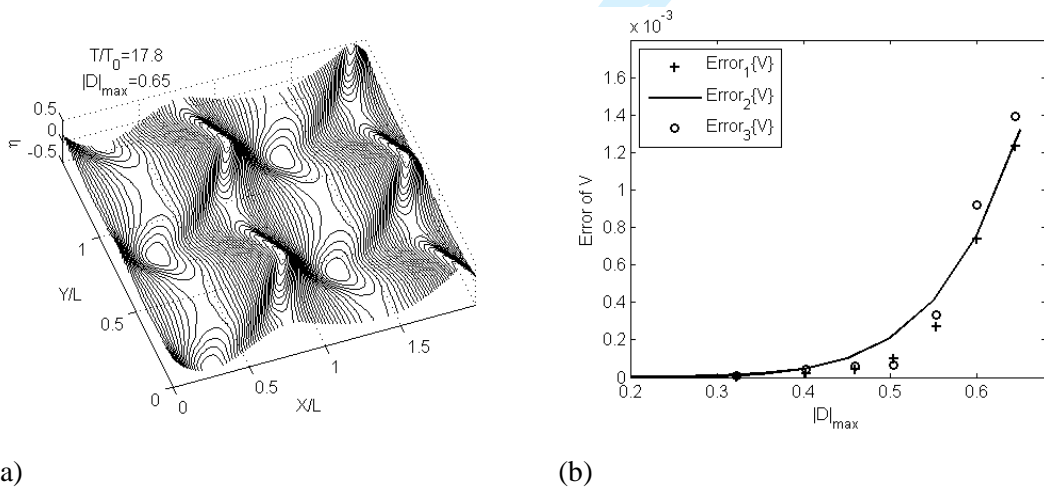


(a) (b)
Figure 19. Wave profiles at different instants (a) and numerical error against maximum gradient (b)

The third case considered is about a wave of $\varepsilon = 0.2985$ generated as in Figure 6 but perturbed by a directional side-band waves

$$\delta\eta = \frac{0.05\varepsilon}{2} [\sin(\mathbf{K}_1 \cdot \mathbf{X}) + \sin(\mathbf{K}_2 \cdot \mathbf{X})] \tag{51}$$

where $\mathbf{K}_1 = (3/2, 4/3)$ and $\mathbf{K}_2 = (3/2, -4/3)$. The computational domain covers $2L \times 1.5L$ on transversal and longitudinal direction and is resolved by $2^8 \times 2^8$ points. The duration of the simulation is 18 wave periods. During the simulation, the waves grow into horse-shoe pattern eventually at $T/T_0 = 17.8$, as shown in Figure 20(a). The error of Scheme 2 is shown on the right in Figure 20(b). This again indicates that the error is insignificant when $|D|_{max} \leq 0.5$.



(a) (b)
Figure 20. Wave surface snapshot (left) and error against gradient (right)

All the above cases for different kinds of wave evidence that one may take 0.5 as the critical value (D_c) if the error of $2E-4$ is acceptable, under which Scheme 2 may be applied with ignoring the integral parts in the velocity V . They evidence also that Equations (46) and (47) give a good estimation to the error of Scheme 2, though the former is derived using a higher order term and the latter using very simple waves.

Equation (46) is more general than Equation (47) as the former is not based on specific waves. In practice, one may take $D_c = 0.5$ or use Equation (46) to determine D_c for a specified error. More generally, one may numerically estimate the error by using Equation (46). If using this way, the condition of $|D|_{max} \leq D_c$ in Figure 2 must be replaced by $Error_1\{V\} \leq Error_c$, where $Error_c$ is the tolerant error.

6. OVERALL EFFICIENCY OF THE IMPROVED METHOD

Up to now, three new techniques have been discussed. They are developed in order to accelerate the computation of the Spectral Boundary Integral Method originally proposed in [1-4]. In this section, the overall efficiency of the improved method equipped with the **de-singularity technique for weakly singular integrals**, the anti-aliasing technique and the mixed scheme (Figure 2) will be discussed. For this purpose, the convergent properties and CPU time of the method in [4] and the improved method of this paper will be compared. Both methods are employed to simulate the waves similar to that in Figure 20 but with different initial steepness, i.e., $\varepsilon = 0.1, 0.2$ and 0.3 , respectively. For each of the cases, different resolutions are used, which are 2^5*2^5 , 2^6*2^6 , 2^7*2^7 and 2^8*2^8 . The simulation is carried out until $T/T_0 = 18$.

For this case, Fructus *et al.* [4] presented a quantitative result of the following ratio for $\varepsilon = 0.2985$

$$\Psi_\varepsilon = \frac{|F\{\eta\}|_{(K=(3/2,4/3),T)}}{|F\{\eta\}|_{(K=(1,0),T=0)}} \quad (52)$$

where $|F\{\eta\}|_{(K=(3/2,4/3),T)}$ is the value of the spectrum at a time T corresponding to the first disturbed term with $K = (3/2, 4/3)$ in Equation (51). Their result is re-produced in Figure 21. We also make a code based on the method in [4] and use it to compute the same case. The result from this code is marked as 'Method in [4]' in Figure 21. Both results are compared with the result from our improved method of the paper in the figure. The resolution we used for this case is 2^8*2^8 . It can be seen that the present method produces almost the same result as the **Method** in [4]. However, the numerical results we calculated are slightly different from the data provided by [4]. The main reason would be due to difference in determining of time steps. The specific equation for estimating the error related to the adaptive step, like Equation (13), was not given in [4]. The time step may be different if the method for estimating the error is not same as Equation (13).

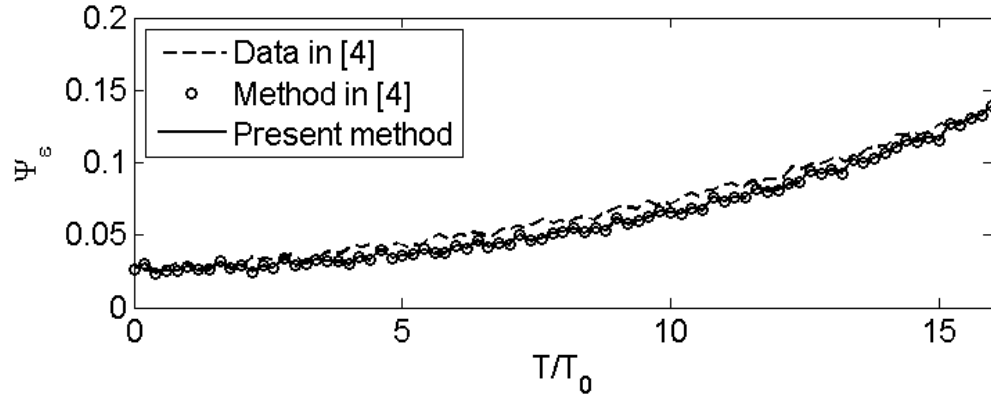
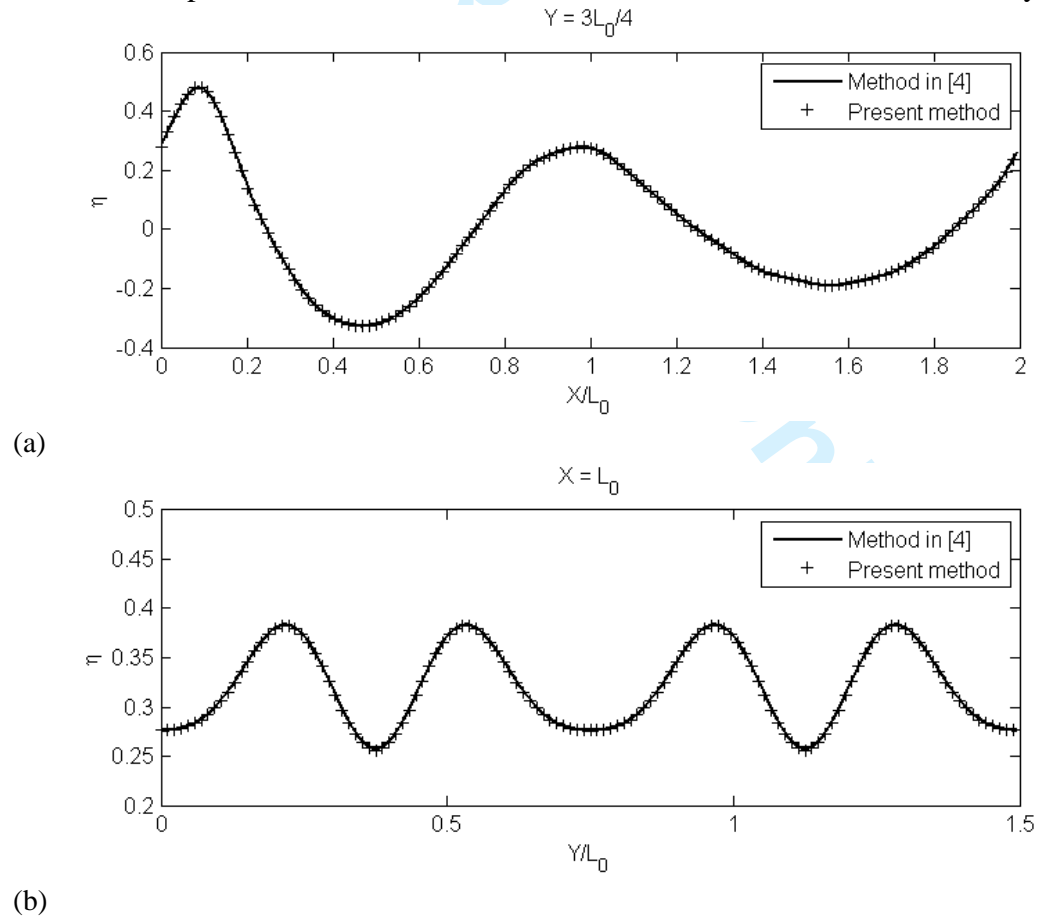
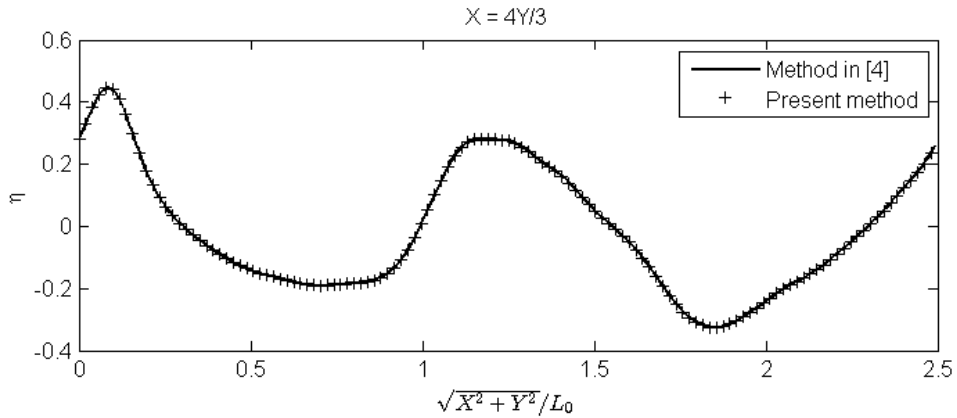


Figure 21. Evolution of perturbation components of $\mathbf{K} = (3/2, 4/3)$

The free surface profiles at three sections ($Y = 3L_0/4$, $X = L_0$ and $X = 4Y/3$) obtained by the code based on the **Method** in [4] and our improved method are shown in Figure 22. There is no visible difference between them. Their quantitative difference is of $\int (|\eta_1 - \eta_2|) d\mathbf{X} / \int |\eta_2| d\mathbf{X} \approx 0.2\%$, where η_1 is the free surface elevation at $T/T_0 = 18$ obtained from the method in [4] and η_2 is that from the improved method, both for resolution of $2^8 \times 2^8$. This demonstrates that both the methods will produce almost the same results when the resolution is sufficiently high.





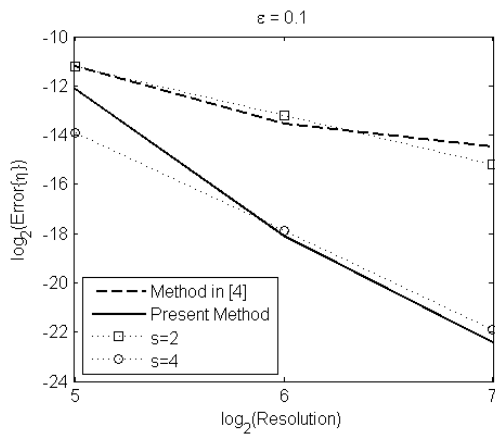
(c)

Figure 22. Free surface profiles at different section for $\epsilon = 0.3$

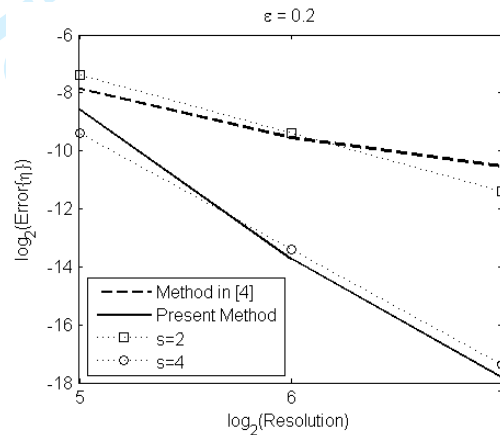
However, their convergent rate may be different. To examine this, we define the error of the wave elevation as

$$Error_2\{\eta\} = \frac{\int (|\eta^{(N=2^n)} - \eta_B|) dX}{\int |\eta_B| dX} \tag{53}$$

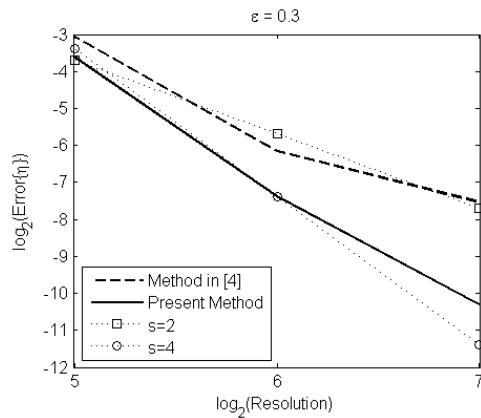
where $\eta^{(N=2^n)}$ is the solution obtained by using a method with resolution $2^n * 2^n$ at $T/T_0 = 18$ and η_B is the solution with sufficiently high resolution. Here η_B is selected as that for Figure 22. The errors of two methods corresponding to different initial steepness are plotted in



(a)



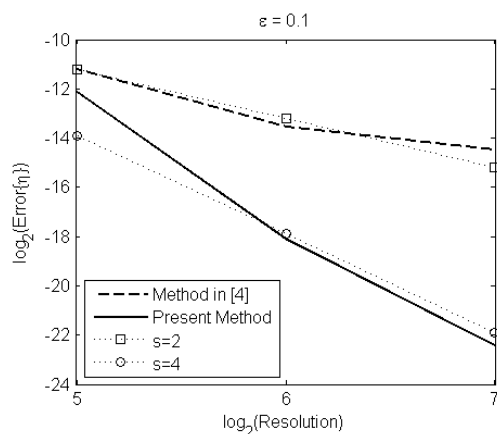
(b)



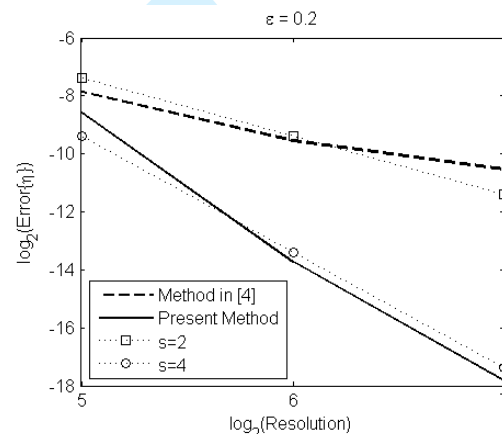
(c)

Figure 233, together with the lines representing $(\Delta X)^s$ where ΔX denotes the element size. It shows that the convergent rate of the improved method is closed to the 4th order for all the cases.

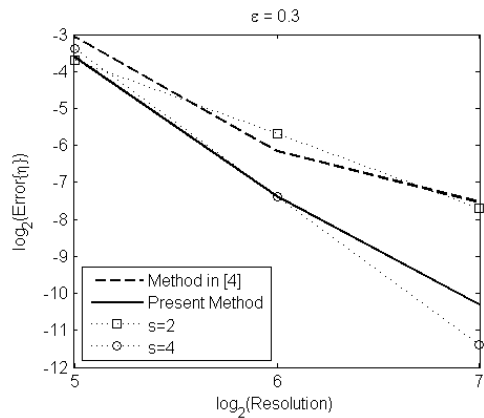
In addition, the CPU time used by the two methods to achieve the results with error less than 0.2% is also investigated. Figure 24 depicts the ratio of the CPU time used by the **Method** in [4] to that of the improved method. It indicates that for waves with moderate steepness ($\epsilon \leq 0.1$), the CPU time of both the methods is similar. When the steepness increases, the advantage of the improve method over the **Method** in [4] is obvious. For instance, in the case of $\epsilon = 0.2985 \approx 0.3$, the ratio is more than 35. Of course, if the requirement on the accuracy is not so high, the CPU time ratio may not be thus large. We do examine the wave profiles with different errors. The profiles along the transversal direction corresponding to different error values are shown in Figure 25. It can be seen that the profile with an error of about 0.6% calculated by Equation (54) would be quite different. The error of about 0.2% is needed to achieve invisible result based on our observation.



(a)



(b)



(c)

Figure 23. Convergent rate of different methods for $\epsilon = 0.1, 0.2$ and 0.3

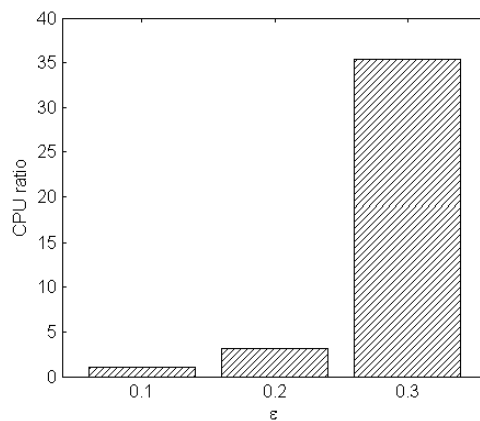


Figure 24. CPU ratio against steepness at error less than 0.2% $X = L_0$

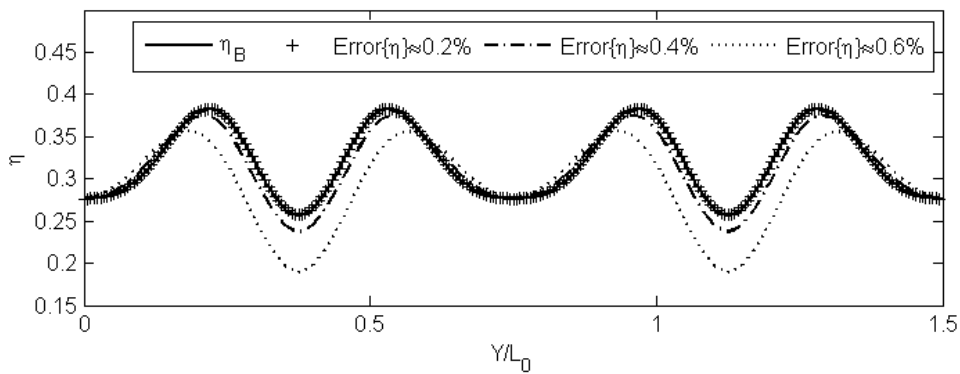


Figure 25. Profiles corresponding to different errors

7. CONCLUSION

This paper presents three numerical techniques in order to improve the computational efficiency of the spectral boundary integral method proposed and developed by Clamond & Grue [1], Grue [2, 3] and Fructus *et al.* [4] for simulating nonlinear water waves. **The techniques** include the de-singularity technique, the anti-aliasing technique and the technique for determining the critical value of the free surface

gradient for the mixed scheme illustrated in Figure 2. It has demonstrated that the improved method equipped with the techniques can significantly accelerate the computation, in particular in the cases with strong nonlinearity. In some cases, it has been observed to be more than 35 time faster than the method without the techniques.

APPENDIX

Equation (19) is re-written as

$$F\{V_3\} = \frac{K}{2\pi} F \left\{ \int_{S_0} \tilde{\phi}' \left[1 - (1 + D^2)^{-3/2} \right] \nabla' \cdot \left[(\eta' - \eta) \nabla' \frac{1}{R} \right] d\mathbf{X}' \right\} \quad \text{A. 1}$$

The term involving in the local gradient is expanded in the Taylor series

$$1 - (1 + D^2)^{-3/2} = \frac{3}{2} D^2 - \frac{15}{8} D^4 + \frac{35}{16} D^6 \dots \quad \text{A. 2}$$

Using it, V_3 becomes

$$\begin{aligned} F\{V_3\} &= \frac{K}{2\pi} F \left\{ \frac{3}{2} \int \tilde{\phi}' D^2 \nabla' \cdot \left[(\eta' - \eta) \nabla' \frac{1}{R} \right] d\mathbf{X}' \right. \\ &\quad - \frac{15}{8} \int \tilde{\phi}' D^4 \nabla' \cdot \left[(\eta' - \eta) \nabla' \frac{1}{R} \right] d\mathbf{X}' \\ &\quad + \int \tilde{\phi}' \left[1 - (1 + D^2)^{-3/2} - \frac{3}{2} D^2 + \frac{15}{8} D^4 \right] \nabla' \\ &\quad \left. \cdot \left[(\eta' - \eta) \nabla' \frac{1}{R} \right] d\mathbf{X}' \right\} \\ &= F\{V_3^{(1)}\} + F\{V_3^{(2)}\} + F\{V_{3,I}\} \end{aligned} \quad \text{A. 3}$$

where

$$\begin{aligned} F\{V_3^{(1)}\} &= -\frac{K}{6} \left[Ki\mathbf{K} \cdot F\{\eta^3 \nabla \tilde{\phi}\} - 3F\{\eta F^{-1}\{Ki\mathbf{K} \cdot F\{\eta^2 \nabla \tilde{\phi}\}\}\} \right. \\ &\quad \left. + 3F\{\eta^2 F^{-1}\{Ki\mathbf{K} \cdot F\{\eta \nabla \tilde{\phi}\}\}\} + F\{\eta^3 F^{-1}\{K^3 F\{\tilde{\phi}\}\}\} \right] \end{aligned} \quad \text{A. 4}$$

and

$$\begin{aligned} F\{V_3^{(2)}\} &= -\frac{K}{120} \left[i\mathbf{K}K^3 \cdot F\{\eta^5 \nabla \tilde{\phi}\} - 5F\{\eta F^{-1}\{i\mathbf{K}K^3 \cdot F\{\eta^4 \nabla \tilde{\phi}\}\}\} \right. \\ &\quad + 10F\{\eta^2 F^{-1}\{i\mathbf{K}K^3 \cdot F\{\eta^3 \nabla \tilde{\phi}\}\}\} \\ &\quad - 10F\{\eta^3 F^{-1}\{i\mathbf{K}K^3 \cdot F\{\eta^2 \nabla \tilde{\phi}\}\}\} \\ &\quad + 5F\{\eta^4 F^{-1}\{i\mathbf{K}K^3 \cdot F\{\eta \nabla \tilde{\phi}\}\}\} \\ &\quad \left. + F\{\eta^5 F^{-1}\{K^5 F\{\tilde{\phi}\}\}\} \right] \end{aligned} \quad \text{A. 5}$$

Both Equations A. 4 and A. 5 differ from these by Grue [3], though it can be proven that they are equivalent. The corresponding equations in Grue [3] contain 7 and 11

terms in $V_3^{(1)}$ and $V_3^{(2)}$, respectively. Therefore the equations above need less calculation.

In order to estimate the leading order of $V_{3,I}$, the expansion goes further to the 8th order convolution

$$\begin{aligned}
 F\{V_{3,I}\} &= \frac{K}{2\pi} F \left\{ \frac{35}{16} \int \tilde{\phi}' \nabla' \cdot \left[(\eta' - \eta) \nabla' \frac{1}{R} \right] D^6 d\mathbf{X}' \right. \\
 &\quad \left. + \int \tilde{\phi}' \left[1 - (1 + D^2)^{-3/2} - \frac{3}{2} D^2 + \frac{15}{8} D^4 - \frac{35}{16} D^6 \right] \nabla' \right. \\
 &\quad \left. \cdot \left[(\eta' - \eta) \nabla' \frac{1}{R} \right] d\mathbf{X}' \right\} \tag{A.6} \\
 &= F\{V_3^{(3)}\} + \frac{K}{2\pi} F \left\{ \int \tilde{\phi}' \left[1 - (1 + D^2)^{-3/2} - \frac{3}{2} D^2 + \frac{15}{8} D^4 - \frac{35}{16} D^6 \right] \nabla' \right. \\
 &\quad \left. \cdot \left[(\eta' - \eta) \nabla' \frac{1}{R} \right] d\mathbf{X}' \right\}
 \end{aligned}$$

where

$$\begin{aligned}
 F\{V_3^{(3)}\} &= \frac{K}{2\pi} F \left\{ \frac{35}{16} \int \tilde{\phi}' \nabla' \cdot \left[(\eta' - \eta) \nabla' \frac{1}{R} \right] D^6 d\mathbf{X}' \right\} \\
 &= -\frac{K}{5040} \left[i\mathbf{K}\mathbf{K}^5 \cdot F\{\eta^7 \nabla \tilde{\phi}\} - 7F\left\{\eta F^{-1}\left\{i\mathbf{K}\mathbf{K}^5 \cdot F\{\eta^6 \nabla \tilde{\phi}\}\right\}\right\} \right. \\
 &\quad \left. + 21F\left\{\eta^2 F^{-1}\left\{i\mathbf{K}\mathbf{K}^5 \cdot F\{\eta^5 \nabla \tilde{\phi}\}\right\}\right\} \right. \\
 &\quad \left. - 35F\left\{\eta^3 F^{-1}\left\{i\mathbf{K}\mathbf{K}^5 \cdot F\{\eta^4 \nabla \tilde{\phi}\}\right\}\right\} \right. \tag{A.7} \\
 &\quad \left. + 35F\left\{\eta^4 F^{-1}\left\{i\mathbf{K}\mathbf{K}^5 \cdot F\{\eta^3 \nabla \tilde{\phi}\}\right\}\right\} \right. \\
 &\quad \left. - 21F\left\{\eta^5 F^{-1}\left\{i\mathbf{K}\mathbf{K}^5 \cdot F\{\eta^2 \nabla \tilde{\phi}\}\right\}\right\} \right. \\
 &\quad \left. + 7F\left\{\eta^6 F^{-1}\left\{i\mathbf{K}\mathbf{K}^5 \cdot F\{\eta \nabla \tilde{\phi}\}\right\}\right\} + F\left\{\eta^7 F^{-1}\left\{K^7 F\{\tilde{\phi}\}\right\}\right\} \right\}
 \end{aligned}$$

Therefore

$$\begin{aligned}
 V_3^{(3)} &= -\frac{1}{5040} F^{-1} \left\{ i\mathbf{K}\mathbf{K}^6 \cdot F\{\eta^7 \nabla \tilde{\phi}\} - 7KF \left\{ \eta F^{-1} \left\{ i\mathbf{K}\mathbf{K}^5 \cdot F\{\eta^6 \nabla \tilde{\phi}\} \right\} \right\} \right. \\
 &\quad \left. + 21KF \left\{ \eta^2 F^{-1} \left\{ i\mathbf{K}\mathbf{K}^5 \cdot F\{\eta^5 \nabla \tilde{\phi}\} \right\} \right\} \right. \\
 &\quad \left. - 35KF \left\{ \eta^3 F^{-1} \left\{ i\mathbf{K}\mathbf{K}^5 \cdot F\{\eta^4 \nabla \tilde{\phi}\} \right\} \right\} \right. \tag{A.8} \\
 &\quad \left. + 35KF \left\{ \eta^4 F^{-1} \left\{ i\mathbf{K}\mathbf{K}^5 \cdot F\{\eta^3 \nabla \tilde{\phi}\} \right\} \right\} \right. \\
 &\quad \left. - 21KF \left\{ \eta^5 F^{-1} \left\{ i\mathbf{K}\mathbf{K}^5 \cdot F\{\eta^2 \nabla \tilde{\phi}\} \right\} \right\} \right. \\
 &\quad \left. + 7KF \left\{ \eta^6 F^{-1} \left\{ i\mathbf{K}\mathbf{K}^5 \cdot F\{\eta \nabla \tilde{\phi}\} \right\} \right\} + KF \left\{ \eta^7 F^{-1} \left\{ K^7 F\{\tilde{\phi}\} \right\} \right\} \right\}
 \end{aligned}$$

For $\eta = \varepsilon \cos X$, $\tilde{\phi} = \varepsilon \sin X$ and $V = \varepsilon \sin X$, one obtains that

$$V_3^{(3)} = -\frac{1}{5040} \frac{\varepsilon^8}{128} [-17388 \sin(2X) + 3024 \sin(4X) - 12 \sin(6X)] \quad \text{A. 9}$$

$$\sim \frac{69}{2560} \varepsilon^8 \sin(2X)$$

Similarly, the local gradient term of V_4 in Equation (20),

$$V_4 = F^{-1} \left\{ \frac{K}{2\pi} F \left\{ \int_{s_0} \frac{V'}{R} \left(1 - \frac{1}{\sqrt{1+D^2}} \right) dX' \right\} \right\} \quad \text{A. 10}$$

can also be expanded in the Taylor series

$$1 - \frac{1}{\sqrt{1+D^2}} = \frac{1}{2} D^2 - \frac{3}{8} D^4 + \frac{5}{16} D^6 + \dots \quad \text{A. 11}$$

Then this integration of V_4 could be rewritten as

$$F\{V_4\} = \frac{K}{2\pi} F \left\{ \int \frac{V'}{R} \frac{1}{2} D^2 dX' - \int \frac{V'}{R} \frac{3}{8} D^4 dX' + \int \frac{V'}{R} \frac{5}{16} D^6 dX' \right. \\ \left. + \int \frac{V'}{R} \left(1 - \frac{1}{\sqrt{1+D^2}} - \frac{1}{2} D^2 + \frac{3}{8} D^4 - \frac{5}{16} D^6 \right) dX' \right\} \quad \text{A. 12}$$

$$= F\{V_4^{(1)}\} + F\{V_4^{(2)}\} + F\{V_4^{(3)}\} + F\{V_{4,l}\}$$

where

$$F\{V_4^{(1)}\} = -\frac{K}{2} \left[KF\{\eta^2 V\} - 2F\{\eta F^{-1}\{KF\{\eta V\}\}\} \right. \\ \left. + F\{\eta^2 F^{-1}\{KF\{V\}\}\} \right] \quad \text{A. 13}$$

$$F\{V_4^{(2)}\} = -\frac{K}{24} \left[K^3 F\{V\eta^4\} - 4F\{\eta F^{-1}\{K^3 F\{V\eta^3\}\}\} \right. \\ \left. + 6F\{\eta^2 F^{-1}\{K^3 F\{V\eta^2\}\}\} \right. \\ \left. - 4F\{\eta^3 F^{-1}\{K^3 F\{V\eta\}\}\} + F\{\eta^4 F^{-1}\{K^3 F\{V\}\}\} \right] \quad \text{A. 14}$$

$$F\{V_4^{(3)}\} = \frac{-K}{720} \left[K^5 F\{V\eta^6\} - 6F\{\eta F^{-1}\{K^5 F\{V\eta^5\}\}\} \right. \\ \left. + 15F\{\eta^2 F^{-1}\{K^5 F\{V\eta^4\}\}\} \right. \\ \left. - 20F\{\eta^3 F^{-1}\{K^5 F\{V\eta^3\}\}\} \right. \\ \left. + 15F\{\eta^4 F^{-1}\{K^5 F\{V\eta^2\}\}\} \right. \\ \left. - 6F\{\eta^5 F^{-1}\{K^5 F\{V\eta\}\}\} + F\{\eta^6 F^{-1}\{K^5 F\{V\}\}\} \right] \quad \text{A. 15}$$

$F\{V_4^{(1)}\}$ is the same as that in Fructus *et al* [4]. The other two, corresponding to the

5th and 7th order convolutions are consistent with these in Grue [3]. The evaluation of V_4 is implicit due to the involvement of V and needs to be determined by iterations.

ACKNOWLEDGEMENTS

The first author appreciates the financial support provided by China Scholarship Council (PhD program No. 2011633117). The second author would like to acknowledge the support of EPSRC grant (EP/J012858).

REFERENCES

1. D. Clamond and J. Grue. A fast method for fully nonlinear water-wave computations. *J. Fluid Mech.* 2001; **447**: 337-355.
2. J. Grue. On four highly nonlinear phenomena in wave theory and marine hydrodynamics. *Applied Ocean Research* 2002; **24**: 261-274.
3. J. Grue. Computation formulas by FFT of the nonlinear orbital velocity in three-dimensional surface wave fields. *J. Eng. Math.* 2010; **67**: 55-69,.
4. D. Fructus, D. Clamond, J. Grue and O. Kristiansen. An efficient model for three-dimensional surface wave simulations Part I: Free space problems. *Journal of Computational Physics* 2005; **205**: 665-685,.
5. G. B. Airy. Tides and waves. *London: Encyclopaedia Metropolitana* 1845.
6. H. Lamb. Hydrodynamics (Fourth Edition). Cambridge: Cambridge University Press, 1916.
7. J. Lighthill. Waves in Fluids. *London: Cambridge University Press* 1978.
8. G. G. Stokes. On the theory of oscillatory waves. *Mathematical and Physical Papers* 1847, London, Cambridge University Press.
9. A. C. J. Vastano and J. C. H. Mungall. Theory of waves and surges which propagate the length of a horizontal rectangular canal, imparting to the fluid contained within the canal velocities that are sensibly the same from the top to the bottom [English translation of Boussinesq(1872)]. *College of Geosciences, Texas A&M Univ. Rep. 76-2-T*, 1976.
10. D. J. Korteweg and G. DE Vries. On the change of form of long waves advancing in a rectangular cannal, and on a new type of long stationary waves. *Phil. Mag.* 1895; **39**: 422-443.
11. T. B. Benjamin and J. E. Feir. The disintegration of wave trains on deep water Part 1. Theory. *J. Fluid Mech.* 1967; **2**: 417-430.
12. D. J. Benney and G. J. Roskes. Wave instabilities. *Studies in Applied Mathematics* 1969; **48**: 377-385.
13. V. H. Chu and C. C. Mei. On slowly-varying Stokes waves. *J. Fluid Mech* 1970; **41**: 873-887.

14. A. Davey and K. Stewartson. On three-dimensional packets of surface waves. *Proc. R. Soc. Lond. A* 1974; **388**: 101-110.
15. H. Hasimoto and H. Ono. Nonlinear modulation of gravity waves. *Journal of the Physical Society of Japan* 1972; **33**: 805-811.
16. K. B. Dysthe and K. Trulsen. The evolution of an evolution equation. *Nizhny Novgorod*, 2001.
17. V. E. Zakharov. Stability of periodic waves of finite amplitude on the surface of a deep fluid. *Sov. Phys. J. Appl. Mech. Tech. Phys* 1968; **9**: 86-94.
18. M. S. Longuet-Higgins and E. D. Cokelet. The deformation of steep surface waves on water. I. A numerical method of computation. *Proc. R. Soc. Lond. A* 1976; **350**:1-26.
19. S. T. Grilli, J. Skourup and I. A. Svendsen. An efficient boundary element method for nonlinear water waves. *Engineering analysis with boundary elements* 1989; **6**: 97-107.
20. J. W. Dold. An efficient surface-integral algorithm applied to unsteady gravity waves. *Journal of Computational Physics* 1992; **103**: 90-115.
21. S. T. Grilli, P. Guyenne and F. Dias. A fully non-linear model for three-dimensional overturning waves over an arbitrary bottom. *International Journal for Numerical Methods in Fluids* 2001; **35**: 829-867.
22. G. X. Wu and R. Eatock-Taylor. Finite element analysis of two dimensional non-linear transient water waves. *Appl. Ocean Res.* 1994; **16**: 363-372.
23. G. X. Wu and R. Eatock-Taylor. Time stepping solution of the two dimensional non-linear wave radiation problem. *Ocean Eng.* 1995; **22**: 785-798.
24. Q. W. Ma. Numerical simulation of nonlinear interaction between structures and steep waves. *PhD Thesis, Department of Mechanical Engineering, University College London, Uk*, 1998.
25. Q. W. Ma, G. X. Wu and R. Eatock-Taylor. Finite element simulation of fully non-linear interaction between vertical cylinders and steep waves. Part 1: Methodology and numerical procedure. *Int. J. Numer. Meth. Fluids* 2001; **36**: 265-285.
26. Q. W. Ma, G. X. Wu and R. Eatock-Taylor. Finite element simulation of fully non-linear interaction between vertical cylinders and steep waves. Part 2: Numerical results and validation. *Int. J. Numer. Meth. Fluids* 2001; **36**: 287-308.
27. Q. W. Ma and S. Yan. Quasi ALE finite element method for nonlinear water waves. *Journal of Computational Physics* 2006; **212**: 52-72.
28. Yan, S. and Ma, Q.W. Numerical simulation of fully nonlinear interaction between steep waves and 2D floating bodies using QALE-FEM method. *Journal of Computational Physics* 2007; **221(2)**: 666-692.
29. Yan, S, and Ma, Q.W. QALE-FEM for modelling 3D overturning waves. *International Journal for Numerical Methods in Fluids* 2010; **63**: 743 – 768.
30. Ma, Q.W., and Yan, S. QALE-FEM for Numerical Modelling of Nonlinear

- Interaction between 3D Moored Floating Bodies and Steep Waves. *International Journal for Numerical Methods in Engineering* 2009; **78**: 713-756.
31. D. Dommermuth and D. Yue. A high-order spectral method for the study of nonlinear gravity waves. *J. Fluid Mech.* 1987; **184**: 267-288.
 32. D. P. Nicholls. Traveling Water Waves: Spectral Continuation Methods with Parallel Implementation. *Journal of Computational Physics* 1998; **143(1)**: 224-240.
 33. D. Clamond, D. Fructus and J. Grue. A note on time integrators in water-wave simulations. *Journal of Engineering Mathematics* 2007; **58**: 149-156.
 34. J. R. Dormand and P. J. Pince. A family of embedded Runge-Kutta formulae. *Journal of Computational and Applied Mathematics* 1980; **6(1)**: 19-26.
 35. J. D. Fenton. The numerical solution of steady water wave problems. *Comp. Geosci* 1988; **14(3)**: 357-368.
 36. C. Canuto, M. Y. Haussaini, A. Quarteroni and Z. A. Zang. Spectral Methods in Fluid Dynamics. Berlin: Springer-Verlag, 1987.
 37. L. Xu and P. Guyenne. Numerical simulation of three-dimensional nonlinear water waves. *Journal of Computational Physics* 2009; **228(22)**: 8446-8466.
 38. D. Clamond, D. Fructus, J. Grue and O. Kristiansen. An efficient model for three-dimensional surface wave simulations. Part II: Generation and absorption. *Journal of Computational Physics* 2005; **205**: 686-705.
 39. X. Cai, H. P. Langtangen, B. F. Nielsen and A. Tveito. A finite element method for fully nonlinear water waves. *J. Comp. Physics* 1998; **143**: 544-568.
 40. Grue, J and Fructus, D. Ch 1. Model for fully nonlinear ocean wave simulations derived using Fourier inversion of interal equation in 3D. ADVANCES IN NUMERICAL SIMULATION OF NONLINEAR WATER WAVES (ISBN: 978-981-283-649-6 or 978-981-283-649-7) 2010, edited by Ma, Q.W., The world Scientific Publishing Co..